Phase Change Heat Transfer Enhancement Using Engineered Surfaces

by

MIRVAHID MOHAMMADPOUR CHEHRGHANI

Submitted to the Graduate School of Natural Science and Engineering

In partial fulfillment of the requirement for the degree of

Master of Science

Sabanci University

June 2021

Phase Change Heat Transfer Enhancement Using Engineered Surfaces

APPROVED BY:

APPROVAL:

ABSTRACT

Phase Change Heat Transfer Enhancement Using Engineered Surfaces

MIRVAHID MOHAMMADPOUR CHEHRGHANI

Mechatronics Engineering, M.S. Thesis, June 2021

Thesis Supervisor: Prof. Dr. Ali Koşar

Keywords: Flow condensation; Droplet distribution; Superhydrophobic surface; Nanostructured surface; Droplet condensation heat transfer; Minichannel; Biphilic surface; Optimum design; Heat transfer enhancement

Condensation is a phase change naturally occurring phenomenon and widely encountered in nature. Condensation plays a vital role in various applications, such as power generation, water collection, desalination, electronics cooling. During the last decade, the studies on condensation have been mostly limited to the working conditions, which are ideal for Electron Microscopy techniques. Therefore, the behavior of condensed droplets in the presence of vapor flow with different vapor qualities and their implementation to flow condensation heat transfer enhancement have received rather little attention. In this thesis, two different types of surfaces, namely superhydrophobic and biphilic surfaces, have been investigated. First, on superhydrophobic surfaces, besides heat transfer analysis, we performed a visualization study during flow condensation in a minichannel and investigated droplet dynamics including a histogram of droplet diameter distribution at different time intervals and stages of a condensation cycle consisting of nucleation growth and departure, droplet departure diameters, cycle time, and droplet number density. The droplet departure diameter decreases with steam mass flux, leading to a shift to smaller radii in droplet size distribution, which enhances condensation heat transfer.

Enhancements up to 33% in heat transfer coefficient were obtained at lower steam qualities for the tested superhydrophobic surface compared to the reference plain hydrophobic surface. Secondly, to take advantage of the mixed wettability, we fabricated biphilic surfaces to assess their effect on heat transfer performance during flow condensation. Electron beam physical vapor deposition (PVD) technique was utilized to form hydrophobic patterns on the superhydrophobic substrate. Here, we report an optimum island diameter D of the hydrophobic spots on a superhydrophobic substrate, where heat transfer performance becomes maximum. We show that considering the optimum islands diameter, compared to the plain hydrophobic surface, condensation heat transfer coefficient is enhanced by 51, 48, 42, 40, and 36% for the steam mass flux of 10, 20, 30, 40, and 50 kg/m²s, respectively. Through visualization experiments, we demonstrate that the observed optimum points correspond to enhanced droplet nucleation and rapid sweeping region, where droplet pinning and bridging do not occur. By fitting the experimental data, a correlation for the prediction of the optimum island diameter of biphilic surfaces is provided as a function of steam mass flux for flow condensation heat transfer.

ÖZET

Yüzey Mühendisliği İle Faz Değişimi Isı Transferi Geliştirme

MIRVAHID MOHAMMADPOUR CHEHRGHANI

Mekatronik Mühendisliği YÜKSEK LİSANS TEZİ, Haziran 2021

Tez Danışmanı: Prof. Dr. Ali Koşar

Anahtar Kelimeler: Akış yoğunlaşması; Damlacık dağılımı; Süperhidrofobik yüzey; Nano yapılı yüzey; Damlacık yoğuşma ısı transferi; Mini kanal; Bifilik yüzey; Optimum tasarım; Isı transferi geliştirme

Yoğuşma, doğal olarak meydana gelen ve doğada yaygın olarak karşılaşılan bir faz değişimi olayıdır. Yoğuşma, enerji üretimi, su toplama, tuzdan arındırma, elektronik soğutma gibi çeşitli uygulamalarda hayati bir rol oynar. Son on yılda, yoğuşma üzerine yapılan çalışmalar çoğunlukla Elektron Mikroskobu teknikleri için ideal olan çalışma koşullarıyla sınırlı kalmıştır. Bu nedenle, farklı buhar kalitesine sahip buhar akışı varlığında yoğuşmuş damlacıkların davranışı ve bunların akış yoğuşma ısı transferini arttırmaya uygulanması oldukça az ilgi görmüştür. Bu tezde süperhidrofobik ve bifilik olmak üzere iki farklı yüzey türü incelenmiştir. İlk olarak, süperhidrofobik yüzeylerde, ısı transferi analizinin yanı sıra, bir minikanalda akış yoğuşması sırasında bir görselleştirme çalışması gerçekleştirilmiştir. Çekirdeklenme büyümesi ve ayrılmasından oluşan bir yoğuşma döngüsünün farklı zaman aralıklarında ve aşamalarında damlacık çapı dağılımının bir histogramını içeren damlacık dinamikleri araştırılmıştır. Damlacık ayrılma çapları, döngü süresi ve damlacık sayısı yoğunluğu bulunmuştur. Damlacık çıkış çapı buhar kütle akışı ile azalmış, bu da damlacık boyutu dağılımında daha küçük yarıçaplara kaymaya yol açmıştır. Böylelikle yoğuşma ısı transferi artırılmıştır. Referans düz hidrofobik yüzeye kıyasla test edilen süperhidrofobik yüzey için daha düşük buhar kalitelerinde ısı transfer katsayısında %33'e varan iyileştirmeler elde edilmiştir. İkinci olarak, karışık ıslanabilirlikten yararlanmak için,

akış yoğuşması sırasında ısı transfer performansı üzerindeki etkilerini değerlendirmek için bifilik yüzeyler üretilmiştir. Süperhidrofobik yüzey üzerinde hidrofobik desenler oluşturmak için elektron ışını fiziksel buhar biriktirme (PVD) tekniği kullanılmıştır. Burada, ısı transfer performansının maksimum olduğu bir süperhidrofobik yüzey üzerindeki hidrofobik noktaların D çapı optimum adacıklarını rapor edilmiştir. Optimum ada çapı dikkate alındığında, düz hidrofobik yüzeye kıyasla, yoğuşma ısı transfer katsayısının 10 , 20, 30, 40 ve 50 kg/m^{2}s buhar kütle akışı için sırasıyla %51, 48, 42, 40 ve 36 oranında arttığı rapor edilmiştir. Görselleştirme deneyleri yoluyla, gözlemlenen optimum noktaların, damlacık sabitleme ve köprülemenin meydana gelmediği gelişmiş damlacık çekirdeklenmesine ve hızlı süpürme bölgesine karşılık geldiğini gösterilmiştir. Deneysel verilere uygun olarak, akış yoğuşma ısı transferi için buhar kütle akışının bir fonksiyonu olarak bifilik yüzeylerin optimum ada çapının tahmin edilmesi için bir korelasyon geliştirilmiştir.

ACKNOWLEDGEMENTS

This thesis is dedicated to my beloved family

TABLE OF CONTENTS

LIST OF FIGURES

LIST OF TABLES

1   INTRODUCTION

1.1   Overview of Condensation Heat Transfer

The Condensation is one of the fundamental phase change phenomena widely encountered in nature[1]. Condensation heat transfer enhancement plays a vital role in energy and cost reduction in the industry. Emerging applications include water harvesting and desalination systems[2,3], electronics cooling[4] especially in high performance supercomputers, power generation systems[5], heat exchangers[6], building thermal systems[7], and electric automobile battery thermal management systems[8]. Depending on the wettability behavior of condensing surfaces, condensation can be classified into two categories: film and dropwise condensation[9]. Film condensation, which is characterized by the formation of liquid film on the solid surface, mostly takes place on wetting (hydrophilic) surfaces. In contrast, dropwise condensation, which is distinguished by discrete droplet formation and removal, is promoted by (super)hydrophobic (non-wetting) surfaces[10]. By providing droplet mobility and rapid surface refreshing, dropwise condensation remarkably enhances the condensation heat transfer performance.

1.2   Condensation Heat Transfer on Nanostructures Superhydrophobic Surfaces

After the pioneering study of Schmidt et al.[11], where a substantially higher thermal performance was reported compared to film condensation, dropwise condensation has attracted the attention of many engineers and scientists[12–14].

So far, the focus has been on reducing the surface wettability to promote dropwise condensation[15–17]. Continuous dropwise condensation and rapid removal of condensate droplets on engineered two-tier textured superhydrophobic surfaces were investigated for their potential to enhance condensation heat transfer[15]. In this regard, micropillars (first roughness elements) were etched in silicon by the deep reactive ion etching method. The second roughness elements (deposited CNT nanopillars) were formed via plasma enhanced chemical vapor deposition. A significant increase in droplet renewal frequency on a structured superhydrophobic surface compared to a nanostructured hydrophobic surface was reported using the environmental electron microscopy (ESEM) [16], where a superhydrophobic surface was obtained by combination of

nanostructures and decreasing the surface energy. In another study[17], Self-Assembled Monolayer (SAM) coated copper tubes and SAM-on-gold-coated-aluminum tubes led to 14 times and 9 times enhancements compared to film condensation, respectively[17]. However, nanotexturing not always offered the best thermal performance[18]. Smaller droplet departure diameter and higher droplet departure frequency on the SAM coated plain surface were reported compared to the nanotextured surface by Zhang et al[18], which was attributed to condensate and surface interfacial interactions. A comparative study between a two-tier roughness surface consisting of nanowires on micropyramids and single level structured surfaces for condensation under the ambient condition showed that the two-tier surface with nanowires on micropyramids yielded superior droplet mobility under both wet (condensation) and dry conditions[19]. Due to the structures on micropyramids of two-tier surface, droplets showed lower adhesion to the pyramid side, and the transition from Cassie to Wenzel state was avoided.

The abovementioned studies on droplet condensation involve large and unlimited spaces, which are focused on steam droplet condensation neglecting vapor shear. In those scenarios the main droplet detachment mechanism is governed by the gravity or coalescence-induced jumping. However, during flow condensation, vapor shear is the dominant droplet departure mechanism. Therefore, reducing the channel cross sectional area helps increase vapor mass fluxes and obtain higher vapor shear rates. To investigate the potential of hydrophobic surfaces for enhancing the steam flow condensation heat transfer performance in minichannels and microchannels, some studies could be found in the literature[20–25]. In the study of Fang et al .[19], flow visualization and heat transfer analysis of flow condensation of pure steam were performed in a rectangular microchannel, and a strong dependency of flow patterns on wall wetting properties were reported[20]. Derby et al. [21] investigated steam flow condensation in a minichannel with various biphilic patterns for steam mass fluxes in the range of 50 to 200 kg/m^2s and a wide range of steam qualities. While both plain hydrophobic and biphilic surfaces provided enhancements in the thermal performance compared to the bare hydrophilic surface, the best thermal performance was observed for the plain hydrophobic surface. Chen and Derby[23] extended Derby's previous work[21] , and their heat transfer analysis and visualization study on a minichannel revealed enhancements in the thermal performance of hydrophobic surfaces, as a result of the increased droplet mobility. Another study by Chen et al.[24] on flow condensation heat transfer inside a minichannel with a hydrophobic surface in the presence of non-condensable gasses (NCG) revealed that NCG reduced

the thermal performance of the system by 24 to 55%, which was due to the accumulation of NCG pockets on the condensing surface.

Recently, innovative studies with the potential in condensation heat transfer enhancement have been introduced. Biphilic surfaces were used to take advantage of combined film and dropwise condensation[26]. It was shown that superhydrophilic regions on biphilic surfaces promoted the heat transfer performance by reducing the delay in neighboring droplet coalescence. Condensation experiments on hybrid superhydrophobic and hydrophilic surfaces fabricated with a combination of wet etching and laser ablation methods were performed[27]. Accordingly, the distance between hydrophilic islands affected both droplet growth rate and coalescence-induced droplet departure and was an important parameter for enhancing condensation heat transfer. In addition, the Lattice Boltzmann method has been applied in multiphase flows and phase change heat transfer [28,29]. Moreover, in recent studies regarding the Lattice Boltzmann phase change model, surfaces with heterogeneous mixed wettability[30], different wettability[31], and textured structures[32] were considered for condensation heat transfer.

Extensive studies on the effect of surface wettability on flow condensation heat transfer with mixtures[33,34] and refrigerants[35–37]exist in the literature. Higher heat transfer coefficients were obtained in flow condensation of the refrigerant R1234ze(E) in minichannels compared to conventional size channels[38]. Increased vapor shear stress in minichannels contributed to the thermal performance enhancement in minichannels. Compared to a surface with higher wettability, condensation heat transfer enhancements were reported for R141b on a lower wettability surface[36], and it was demonstrated that an increase in mass flux led to an increase in heat transfer coefficient, which was due to the increase in the shear stress between vapor and liquid. To investigate the effect of fins in a rectangular minichannel with hydraulic diameters of 0.64- and 0.81-mm, Rahman et al. [37] performed an experimental study and showed that an increase in refrigerant mass flux, vapor quality and presence of fins yielded enhancements in the condensation heat transfer performance.

Due to their excellent water repellency and dewetting characteristic, superhydrophobic surfaces were preferred in many studies on condensation heat transfer[39–48]. Miljkovic et al. [49] made the use of combination of nanotexturing and reducing the surface energy on pure copper tubes to obtain superhydrophobic nanostructured surfaces. They demonstrated that coalescence-induced droplet jumping on nanotextured superhydrophobic surfaces yielded a heat transfer enhancement of 30% relative to conventional dropwise condensation on plain hydrophobic surfaces. Coalescence-

induced droplet jumping on nanotextured superhydrophobic surfaces was attributed to the release of excess surface energy and was independent of the gravity[50]. In a more recent study, the effect of microstructure density, which was defined as the number of microflowers within a specified area, was investigated on a copper-based superhydrophobic surface for enhancing condensation heat transfer[51]. Enhancement in condensation heat transfer with microflower density was due to the reduction in cycle time and droplet size and increase in droplet nucleation site. Moreover, because of its potential utilization in semiconductor device thermal management systems, superhydrophobic silicon nanowires and aluminum nanostructured surfaces were the main focus of recent studies[52–54]. Silicon nanowires[52], achieved by the wet etching method, yielded 87% enhancement compared to a conventional hydrophobic surface, because of the increase in nucleation sites during dropwise condensation. In addition, pure steam condensation experiments on aluminum superhydrophobic surfaces, which was prepared by three different wet chemical etching techniques,[53] demonstrated that the superhydrophobic surface with higher surface roughness led to the best thermal performance and heat transfer coefficients up to $100\,\mathrm{kW/m^2K}$.

Recently, noteworthy efforts have been made in developing hierarchical superhydrophobic surfaces due to their potential in promoting controlled droplet nucleation and refreshing for enhancing condensation heat transfer performance[55–61]. A 37% performance enhancement was obtained on superhydrophobic surfaces with micropatterned nanowire arrays compared to uniform nanowires, which was due to not only the reduction in droplet departure radius and departure time but also to the increase in droplet density[55]. To investigate the effect of nanostructure topography on the diameter of jumping droplets on a superhydrophobic surface, platinum film thickness, as well as geometrical parameters such as nanostructure pitch distance, pillar height and diameter were altered. [57]. It was demonstrated that a reduction in pitch distance and thickness of the nanostructures decreased critical jumping diameters of the droplets. Wang et al.[59] uncovered the optimum dimensions of interspacing, tip size and height of nanoneedles on a superhydrophobic surface such that condensation heat transfer was enhanced by about 320% compared to a conventional superhydrophobic surface. Their visualization study showed that reducing the nanoneedle spacing was advantageous as it decreased the droplet departure diameter, while an increase in the nanoneedle height and tip-size was not preferred as it increased the droplet departure diameter. In a more recent study, a 100% enhancement in the thermal performance compared to the conventional hydrophobic surface was obtained on a superhydrophobic surface

with networks of nanowires[60]. This high heat transfer performance enhancement was linked the increased droplet mobility, which was promoted by reducing the pitch distance between nanowires.

1.3   Condensation Heat Transfer on Biphilic Surfaces

On the other side, compared to the superhydrophobic surfaces, droplets tend to nucleate easier and faster on the less hydrophobic surfaces[62]. To take advantage of the mixed wettability, biphilic surfaces have been fabricated to investigate their effect on condensation thermal performance. Peng et al. investigated hybrid dropwise-filmwise surfaces with strip configurations for enhancing condensation heat transfer[63]. According to their results the hydrophilic strips removed the condensate droplets from the hydrophobic strips and allowed space for nucleation of new droplets. By optimizing the configuration of strips on the hybrid surfaces the maximum droplet radius and droplet size distribution could be adjust to enhance condensation thermal performance[64]. The ratio of the hydrophobic to hydrophilic strips could also play a vital role in enhancing heat transfer coefficients[65,66]. Optimizing this ratio could enhance condensation thermal performance by controlling droplet departure frequency and droplet area coverage. Tree like hydrophilic patterns on superhydrophobic base with different ratio of the superhydrophobic/hydrophilic area fraction could also be another alternative pattern[67]. The study showed that with the area fraction of 70% approximately 7.4% enhancement in condensation heat transfer performance could be achieved.

In abovementioned studies the hydrophilic strips serve as the drainage path for the condensed droplet. Biphilic surfaces with other patterns, such as circular islands, have shown substantial improvement in condensation heat transfer performance. Due to the spatial control in the droplet nucleation, all the embryos started to nucleate on hydrophilic islands where the condensate droplets were confined on the top of tiny micropillars[68]. Also, flooding, which limits the performance of the superhydrophobic surfaces[49], could be delayed by self-organization of microscale droplets on a hybrid surface[69]. Proper design of hybrid surface, including the islands diameter and pitch distance could enhance condensation thermal performance through the cooperative effects of droplet nucleation, growth, coalescence and departure[70]. Confined growth, coalescence, and jumping of condensate droplets could be simultaneously achieved by the heterogeneously patterned biphilic surfaces[71]. In addition, superhydrophilic region on biphilic

surfaces could promote heat transfer performance by reducing delay in neighboring droplet coalescence[26]. Recently, another study demonstrated that the hydrophilic islands spacing was an important parameter for enhancing condensation heat transfer and influences both droplet growth rate and coalescence-induced droplet departure[27]. It is noteworthy to mention that the application of biphilic surfaces is not limited to condensation heat transfer and has been the focus of research on boiling heat transfer[72,73], and freezing[74] as well. In addition, recently, noteworthy efforts have been made in developing numerical models to investigate hybrid surfaces for their thermal performance and droplet dynamics[75]. Lattice Boltzmann phase change model for surfaces with heterogeneous wettability[30], and textured structures[32] were also considered.

1.4   Novel Aspect

Regarding the study of condensation heat transfer on nanostructures superhydrophobic surfaces introduced in section 1.2, although most of the mentioned studies concentrated on superhydrophobic surfaces and showed a high potential in enhancing the condensation heat transfer performance, the effect of steam flow; therefore, the effect of vapor shear rate was mostly neglected. To the best of authors' knowledge, only Torresin et al.[76] conducted flow condensation experiments on nanostructured superhydrophobic surfaces in a minichannel. They investigated the effect of surface subcooling for three different relatively low steam mass fluxes of 5, 10 and 15 kg/m2s. Even though their study focused on flow condensation heat transfer enhancement with superhydrophobic surfaces, the range of steam mass fluxes was considerably low compared to the studies about hydrophilic and hydrophobic surfaces[21,77–80]. Moreover, while visualization studies solely focused on droplet cycle time, other important visual parameters related to droplet dynamics such as droplet number density, droplet departure diameter, and distribution of droplets on the condensing surface at different steam mass fluxes have not been discussed in detail.

In addition, regarding the study of condensation heat transfer on biphilic surfaces although the mentioned studies in section 1.3 provide valuable information about cooperative effects of biphilic surfaces, the optimum hydrophobic islands on superhydrophobic background and optimum ratio of hydrophobic to superhydrophobic surface areas, which are essential to achieve the best thermal performance, has not been investigated. In addition, the mentioned studies provide insights into the condensation heat transfer performance on various hybrid surfaces where the effect of vapor shear is neglected; however, the studies regarding flow condensation on biphilic surfaces inside a

minichannel, in which the vapor shear force is the governing mechanism for droplet departure, are still scarce.

2   EXPERIMENTAL APPARATUS AND PROCEDURE

2.1   Experimental Setup

In this study, an open-loop system was constructed for steam dropwise flow condensation experiments to determine heat transfer coefficients. The experimental setup consists of four main sections: i) Steam generation equipment; ii) Pre-condenser and post condenser; iii) Test section; and iv) Visualization and data acquisition system.
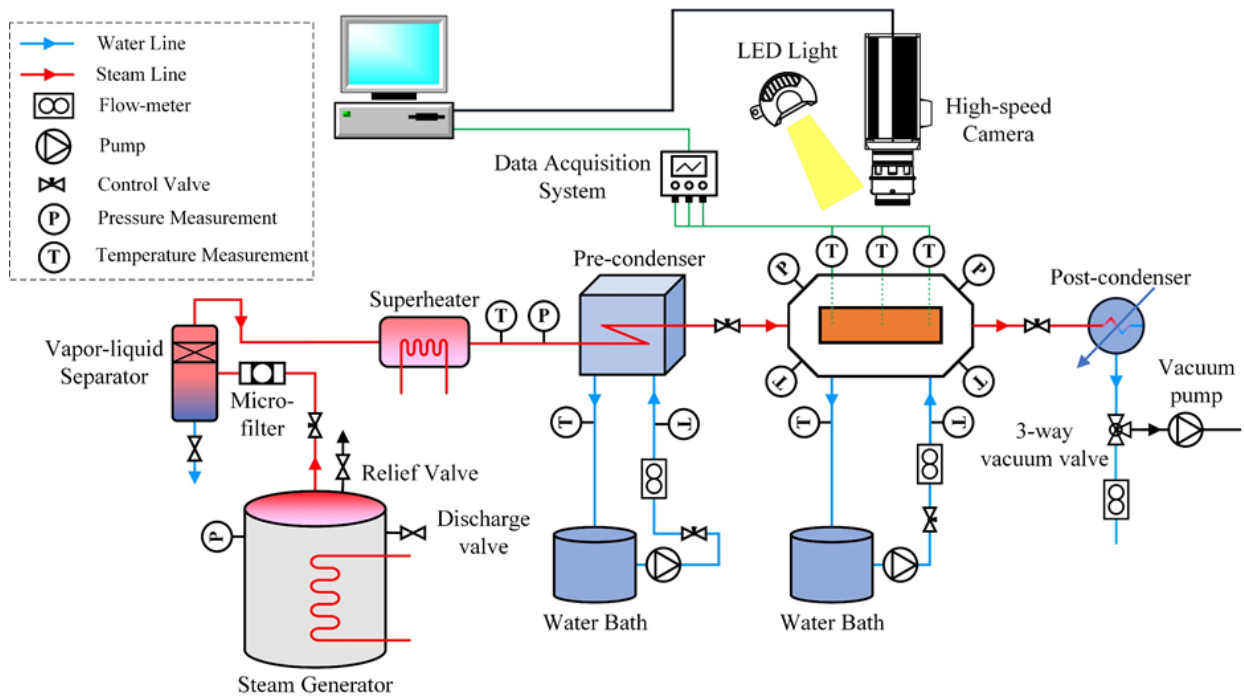
Figure 1. Schematic of the flow condensation experimental setup

The steam generator is equipped with six 1 kW resistance heaters to control the steam mass flux. The pressure inside the steam generator is monitored by a mounted pressure gauge. A control valve is utilized at the outlet of the steam generator to regulate the steam mass flux. The outgoing steam from the steam generator is filtered using 15 μm filters and then passes through a separation tank, which removes the fine liquid droplets inside the saturated steam using a de-entrainment mesh pad. A superheater is utilized to ensure that the steam entering the pre-condenser is

superheated about 1˚C above saturation temperature. The vapor enthalpy at the pre-condenser inlet is determined using its temperature and pressure. In the pre-condenser, the quality of the steam is controlled with the help of a closed-loop cooling water, where the temperature of incoming water is adjusted by a temperature-controlled bath.

The quality of steam entering the test section is estimated using an energy balance between vapor side and cooling side. A separate closed-loop cooling water line is used in the test section to provide heat removal (cooling) from the steam flow. The inlet and outlet temperatures of cooling water (to the pre-condenser and test section) are measured to obtain the quality of steam before and after the test section. After exiting the test section, the steam enters the post condenser, where it could be condensed completely by enabling the mass flow rate to be measured downstream.

All the connections and main parts are insulated by a high thermal insulation material to reduce the heat loss from the system. All the connections and steam pipes are made of stainless steel. T-type thermocouples are mounted at different locations of the flow loop to measure the temperature of the fluid. Moreover, multiple pressure gauges (Omega, USA) are installed at different locations to monitor the pressure. A data acquisition system is used to monitor and record the temperatures of the whole system. A high-speed camera (Phantom VEO-710) is used to visualize and capture real-time images of dropwise flow condensation on the test specimens, where a Veritas miniConstellation 120.28° light-emitting diode (LED) is integrated as the light source to provide the required illumination during visualization.

To minimize the concentration of non-condensable gases (NCG) the following procedure was performed: Before filling the steam generator with deionized DI water, the flow loop was vacuumed for an hour from the end of the flow loop as shown in **Figure 1**, Then, DI water was pumped to the steam generator from a water supply tank. Next, the steam generator was operated, and boiling of DI water inside the steam generator started. After the pressure inside the steam generator increased to above the atmospheric pressure, the discharge valve on the top of the steam generator was opened for several minutes to reduce the remaining content of NCG inside the steam generator. Later, the discharge valve was closed, and the control valve, the valve just after the steam generator, was opened to allow the steam to enter the flow loop. The valve at the end of the flow loop was kept closed until the pressure inside the flow loop reached above the atmospheric pressure. After the whole flow system was pressurized, the valve at the end of the flow loop was

opened. In order to avoid any air from entering the flow loop during the experiments, extreme care was taken to ensure that the system was pressurized.

Experiments were conducted under steady state conditions. First, steam was allowed to enter the system at a desired mass flux. Then, superheater was switched on, ensuring that the superheated steam entered the pre-condenser. Next, the cooling water loops were set at the desired temperatures and flowrates. When the whole system reached steady-state conditions (flow rate, temperatures, pressures, etc.), data acquisition unit was switched on for each experiment. Steam and cooling mass flowrates were recorded using the flowmeters integrated to the system. In the study of "Copper-Based Superhydrophobic Nanostructures for Heat Transfer in Flow Condensation", the experiments were conducted at five different steam mass fluxes of 10, 20, 30, 40 and 50 kg/m^2s for two inlet steam qualities of 0.6 and 0.9 and two cooling water mass flowrates of 2.44 g/s and 9.11 g/s. However, for the work entitled " Biphilic surfaces with optimum islands diameter for heat transfer in flow condensation" five different steam mass fluxes of 10, 20, 30, 40 and 50 kg/m^2s only for inlet steam qualities of 0.9 and cooling water mass flowrates of 9.11 g/s were tested. Steam enters the test section at saturation the pressures and temperatures of 102-130 kPa and 100.2-107.2 °C, respectively, depending on the inlet steam mass flux. A superheater is utilized to ensure that the steam entering the pre-condenser is superheated about 1˚C above the saturation temperature. The vapor enthalpy at the pre-condenser inlet is determined using its temperature and pressure
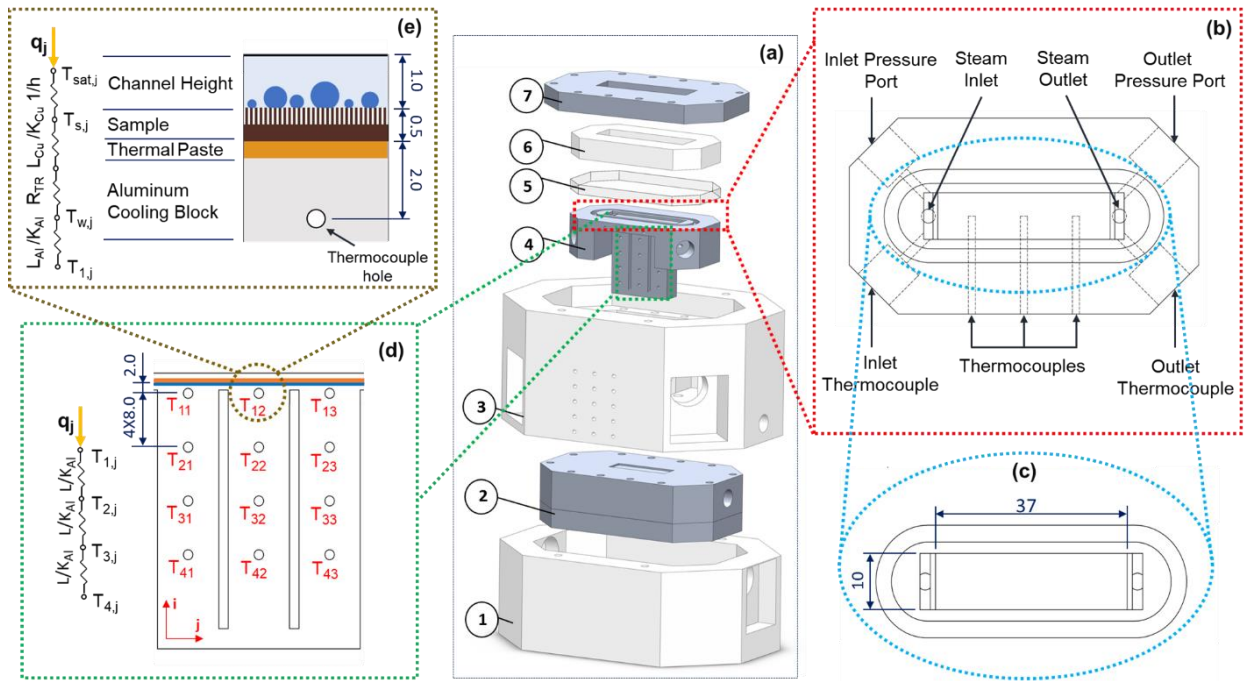
Figure 2. Flow condensation test section (a) Exploded view of the flow condensation test section with the following section: 1) insulating Teflon for the cooling chamber, 2) cooling chamber, 3) insulating Teflon for the aluminum block, 4) condensation block, 5) polycarbonate visualization window, 6) insulating Teflon, 7) aluminum cap. (b) Detailed top view of the condensation block. (c) The schematic showing channel width and length. (d) Thermocouple holes and thermal circuit analysis of the condensation block. Segment number and row number are denoted by subscript j and i, respectively. (e) Surface attachment to the condensation block with thermal paste and corresponding thermal circuit analysis.

Different parts of the test section assembly are shown in **Figure 3**.

2.2 Test Section

Figure 2a shows an exploded view of the flow condensation test section. The visualization window seals the channel from the top and is made of polycarbonate because of its transparency and excellent thermal properties. All components in the test section assembly are sandwiched and fastened by twelve bolts to ensure sealing and perfect thermal contact. A detailed top view of the condensation block is shown in Figure 2b. The condensation block is equipped with inlet and outlet pressure ports for static pressure measurements. In addition, inlet and outlet thermocouples are used to measure the steam temperatures. Figure 2c and e show a more detailed view of the condensation minichannel having dimensions of 10 mm width, 37 mm length and 1 mm height. Twelve T-type thermocouples are inserted into the thermocouple holes having 1 mm diameter with

8 mm distances to determine the heat flux and surface wall temperatures as shown in Figure 2d. By dividing the condensation block into three independent regions, air gaps are formed between each segment. For simplicity, the segment number and row number are denoted by subscript j and i, respectively. As shown in Figure 2e, a high-quality thermal paste between aluminum block and condensation surface ensures a better thermal contact.
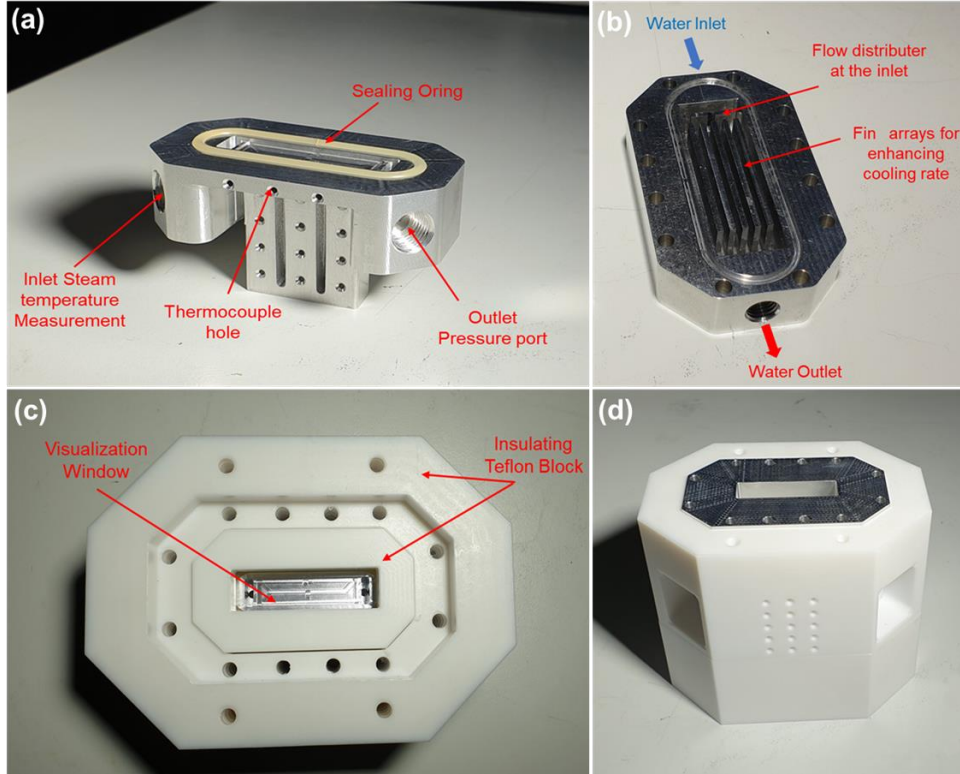
Figure 3. Images of the test section assembly. (a) Condensation block, (b) Cooling block, (c) Insulating Teflon, and (d) Final assembly of the test section.

2.3 Data Reduction and Uncertainty analysis

Mean heat flux q of the condensing block was calculated using the one-dimensional Fourier heat conduction and least squares method:

$$q = \frac{1}{3}\sum_{j=1}^{3} q_j = \frac{1}{3}\sum_{j=1}^{3} -k \frac{\sum_{i=1}^{4}\left(y_{i,j} - \overline{y_j}\right)\left(T_{i,j} - \overline{T_j}\right)}{\sum_{i=1}^{4}\left(y_{i,j} - \overline{y_j}\right)^2} \tag{1}$$

11

where j is the segment number of the block with $j=1$ for the first segment, $j=2$ for the middle segment and $j=3$ for the last segment. i is the row number of thermocouple holes at each segment j as shown in **Figure 4**e . k is the thermal conductivity of the aluminum block. The distance between the center of each thermocouple hole from the first thermocouple hole $y_{1,j}$ is denoted as $y_{i,j}$. The temperature measured on the condensing block at each thermocouple node with row number of i and column or segment number of j are denoted as $T_{i,j}$. Calculated heat flux for each segment j is denoted as q_j.

The mean distance and mean temperature can be calculated as:

$$\left.\begin{aligned} \overline{y_j} &= \frac{1}{4}\sum_{i=1}^{4} y_{i,j} \\ \overline{T_j} &= \frac{1}{4}\sum_{i=1}^{4} T_{i,j} \end{aligned}\right\} \; for \; j=1,2,3 \qquad (2)$$

The surface temperature of the condensing surface for $j=1,2,3$ is expressed as:

$$T_{s,j} = T_{1,j} + q_j\left(\frac{L_{Al}}{k_{Al}} + R_{TP} + \frac{L_{Cu}}{k_{Cu}}\right) \qquad (3)$$

where R_{TP} is the thermal paste resistance. $T_{1,j}$ is the temperature of the first row of segment j as shown in **Figure 4**a. L_{Al} and L_{Cu} are the thickness of the aluminum and copper samples, respectively. The thermal conductivity of aluminum and copper samples are denoted as k_{Al} and k_{Cu}, respectively. Surface temperature (equation S.3) was obtained by establishing an equivalent thermal circuit analysis as shown in **Figure 4**.

The mean heat transfer coefficient can be calculated as:

$$h = \frac{1}{3}\sum_{j=1}^{3} h_j = \frac{1}{3}\sum_{j=1}^{3}\frac{q_j}{T_{sat} - T_{s,j}} \qquad (4)$$

where h_j is the calculated heat transfer coefficient for each segment j. T_{sat} is the steam saturation temperature measured at the inlet of the channel.

Slightly superheated steam ($1°C$ above saturation temperature) enters the precondenser. Pressures and temperatures were measured at the inlet and outlet of both precondenser and main

condensation test section. The quality at the outlet of the precondenser (inlet of the main test section) is calculated as:

$$X_{out} = \frac{h_{st,in} - \dfrac{\dot{m}_{pre,cw} \cdot c_p \cdot \Delta T_{pre,cw}}{\dot{m}_{st}} - h_f}{h_{fg}} \tag{5}$$

where c_p is the specific heat of cooling water and $\dot{m}_{pre,cw}$ is the mass flow rate of the precondenser cooling water measured by the flow meter. $\Delta T_{pre,cw}$ is the temperature difference between inlet and outlet of the precondenser cooling water. $h_{st,in}$ is the enthalpy of the steam at the channel inlet. h_f and h_{fg} are the enthalpy of the saturated liquid at the given pressure and the latent heat released during condensation (enthalpy of vaporization/condensation), respectively. The quality at the outlet of the main test section is calculated with the same methodology described in equation (S.5).

Before performing the experiments, thermocouples were calibrated vis Stirred Liquid Bath Method. An Omega data logger (OM-HL-EH-TC) was used in order to calibrate the T-type thermocouples. The thermocouples were connected to the data logger and submerged into a liquid bath, which was equipped with a temperature controller with a reference probe. A highly conductive paste was used to mount the thermocouples inside the 1 mm diameter holes. The use of this thermal paste ensures the proper contact between the thermocouple head and the aluminum block. The accuracy of measured temperatures at the allocated holes was verified by measuring the surface temperature and calculating the conduction thermal resistance between the surface and the measurement point

13
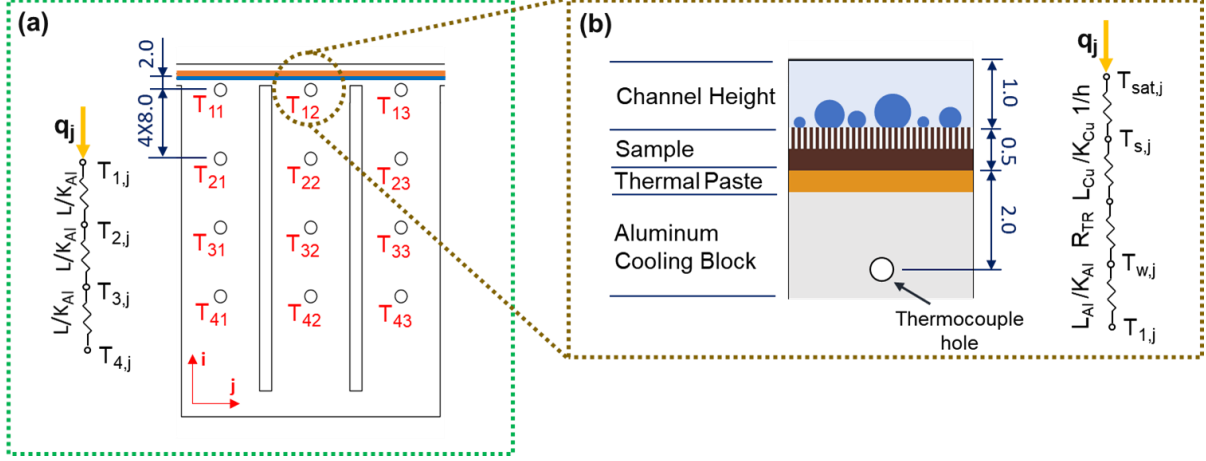
Figure 4. Condensing block. a) Thermocouple holes and thermal circuit analysis of the aluminum block. Segment number and row number are denoted as subscript *j* and *i,* respectively. (b) Surface to the aluminum block attachment with thermal paste and corresponding thermal circuit analysis.

2.4   Uncertainties Analysis

To evaluate the uncertainties in experimental parameters, the spreadsheets supplied by the manufacturers were used. The uncertainties in the measured parameters are displayed in **Table 1**.

Table 1. Measured parameters and uncertainties

Measured Parameters	Uncertainties
Temperature T_{sat}, $T_{i,j}$, T_{cw} [K]	0.15
Pressure P [kPa]	0.1 %
Distance y [mm]	0.2
Thermal conductivity k [w/m^{2}K]	1 %

Using error propagation error methodology[81], the uncertainty of heat flux $\sigma(q_j)$, assuming one-dimensional heat conduction[1] between the two thermocouple planes $q = k\dfrac{\Delta T}{\Delta y}$, is obtained as:

$$\sigma(q_j) = \left\{ \left(\frac{\partial q_j}{\partial k_{Al}} \sigma(k_{Al}) \right)^2 + \left(\frac{\partial q_j}{\partial \Delta T_{(i,\,i+1),j}} \sigma\left(\Delta T_{(i,\,i+1),j}\right) \right)^2 + \left(\frac{\partial q_j}{\Delta y_{(i,\,i+1),j}} \sigma\left(\Delta y_{(i,\,i+1),j}\right) \right)^2 \right\}^{1/2} \tag{6}$$

with $\Delta T_{(i,\,i+1),j} = T_{i,j} - T_{i+1,j}$, the uncertainty of temperature difference between the two thermocouple planes $\sigma\left(\Delta T_{(i,\,i+1),j}\right)$ is calculated as:

$$\sigma\left(\Delta T_{(i,\,i+1),j}\right) = \left\{\left(\frac{\partial \Delta T_{(i,\,i+1),j}}{\partial T_{i,j}}\sigma\left(T_{i,j}\right)\right)^2 + \left(\frac{\partial \Delta T_{(i,\,i+1),j}}{\partial T_{i+1,j}}\sigma\left(T_{i+1,j}\right)\right)^2\right\}^{1/2} \tag{7}$$

Similarly, with $\Delta y_{(i,\,i+1),j} = y_{i,j} - y_{i+1,j}$, the uncertainty of distance between the two thermocouple planes $\sigma\left(\Delta y_{(i,\,i+1),j}\right)$ is calculated as:

$$\sigma\left(\Delta y_{(i,\,i+1),j}\right) = \left\{\left(\frac{\partial \Delta y_{(i,\,i+1),j}}{\partial y_{i,j}}\sigma\left(y_{i,j}\right)\right)^2 + \left(\frac{\partial \Delta y_{(i,\,i+1),j}}{\partial y_{i+1,j}}\sigma\left(y_{i+1,j}\right)\right)^2\right\}^{1/2} \tag{8}$$

The uncertainty of the condensation surface temperature $\sigma\left(T_{s,j}\right)$ is calculated as,

$$\sigma\left(T_{s,j}\right) = \left\{\begin{array}{l} \left(\frac{\partial T_{s,j}}{\partial T_{1,j}}\sigma\left(T_{1,j}\right)\right)^2 + \left(\frac{\partial T_{s,j}}{\partial q_j}\sigma\left(q_j\right)\right)^2 + \left(\frac{\partial T_{s,j}}{\partial T_{1,j}}\sigma\left(T_{1,j}\right)\right)^2 + \left(\frac{\partial T_{s,j}}{\partial L_{Al}}\sigma\left(L_{Al}\right)\right)^2 \cdots \\ \cdots + \left(\frac{\partial T_{s,j}}{\partial k_{Al}}\sigma\left(k_{Al}\right)\right)^2 + \left(\frac{\partial T_{s,j}}{\partial R_{TP}}\sigma\left(R_{TP}\right)\right)^2 + \left(\frac{\partial T_{s,j}}{\partial L_{Cu}}\sigma\left(L_{Cu}\right)\right)^2 + \left(\frac{\partial T_{s,j}}{\partial k_{Cu}}\sigma\left(k_{Cu}\right)\right)^2 \end{array}\right\}^{1/2} \tag{9}$$

Then, the uncertainty of heat transfer coefficient $\sigma\left(h_j\right)$, is estimated as,

$$\sigma\left(h_j\right) = \left\{\left(\frac{\partial h_j}{\partial T_{sat}}\sigma\left(T_{sat}\right)\right)^2 + \left(\frac{\partial h_j}{\partial q_j}\sigma\left(q_j\right)\right)^2 + \left(\frac{\partial h_j}{\partial T_{s,j}}\sigma\left(T_{s,j}\right)\right)^2\right\}^{1/2} \tag{10}$$

The uncertainty of steam quality $\sigma(X)$ is determined as:

$$\sigma(X) = \left\{\left(\frac{\partial X}{\partial \dot{m}_{cw}}\sigma\left(\dot{m}_{cw}\right)\right)^2 + \left(\frac{\partial X}{\partial \dot{m}_{st}}\sigma\left(\dot{m}_{st}\right)\right)^2 + \left(\frac{\partial X}{\partial \Delta T_{cw}}\sigma\left(\Delta T_{cw}\right)\right)^2\right\}^{1/2} \tag{11}$$

where temperature difference in the cooling water is defined by $\Delta T_{cw} = T_{cw,\,out} - T_{cw,\,in}$ and its uncertainty $\sigma(\Delta T_{cw})$ is obtained as:

$$\sigma\left(\Delta T_{cw}\right)=\left\{\left(\frac{\partial\Delta T_{cw}}{\partial T_{cw,\,out}}\sigma\left(T_{cw,\,out}\right)\right)^2+\left(\frac{\partial\Delta T_{cw}}{\partial T_{cw,\,in}}\sigma\left(T_{cw,\,in}\right)\right)^2\right\}^{1/2} \tag{12}$$

where $\sigma\left(\dot{m}_{cw}\right)$ and $\left(\dot{m}_{st}\right)$ are the uncertainty of cooling water and steam mass flow rate according to the specification of the flowmeters provided by the company.

Using the uncertainty propagation methodology[81], the uncertainties in mean heat transfer coefficient and mean vapor quality are found as ±6.6% and ±7.3%, respectively.

2.5 Droplet Thermal Resistance

When the free energy barrier is overcome and the droplet nucleation occurs, growing droplet imposes thermal resistance. For a droplet with radius r on a plain hydrophobic surface these thermal resistances are: resistance due to the curved interface of the droplet R_c, Resistance due to the vapor-liquid interface R_i, condensed droplet conduction resistance R_d, and resistance due to the functional coating R_{fc}.
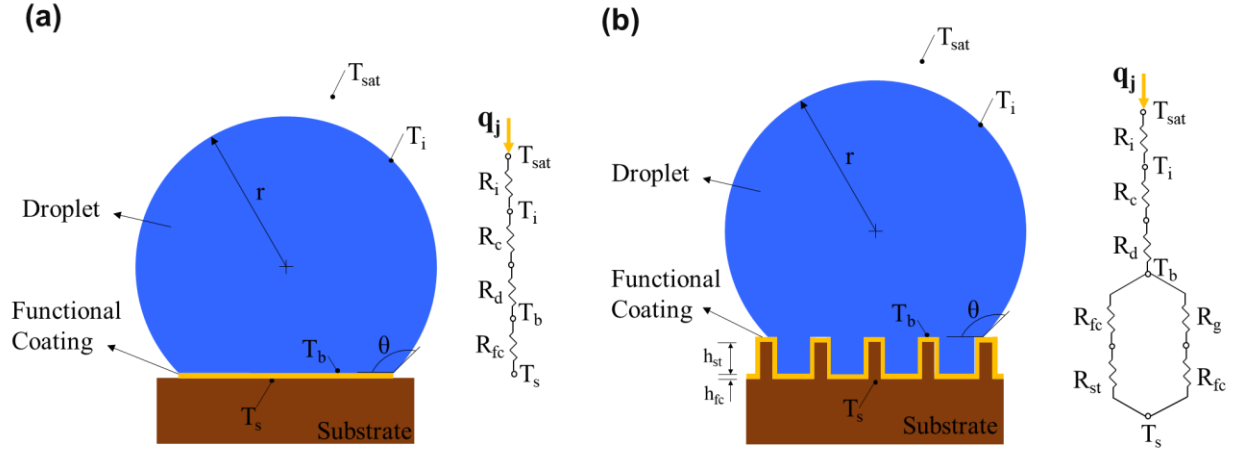
Figure 5. Schematic of the condensed droplet. (a) plain hydrophobic substrate (b) structured superhydrophobic surface (Wenzel morphology)

The resistance due to the curved interface of the droplet R_c can be expressed as,

$$R_c=\frac{2\sigma T_{sat}}{Qrh_{fg}\rho_l} \tag{13}$$

16

where Q is the heat transfer rate trough the droplet, σ is surface tension, T_{sat} is vapor saturation temperature, h_{fg} is latent heat of phase change, and ρ_l is the density of the condensate.

Resistance due to the vapor-liquid interface R_i could be expressed by,

$$R_i = \frac{1}{h_i 2\pi r^2 (1-\cos\theta)} \tag{14}$$

where h_i is interfacial heat transfer coefficient,

$$h_i = \frac{2\alpha}{2-\alpha} \frac{1}{(2\pi R_s T_{sat})^{1/2}} \frac{\rho_v h_{fg}^2}{T_{sat}} \tag{15}$$

where α is condensation coefficient, which ranges from 0-1 depending on the purity of the steam. ρ_l is the vapor density and R_s is specific gas constant.

Condensed droplet conduction resistance R_d is expressed as,

$$R_d = \frac{\theta}{4\pi r k_l \sin\theta} \tag{16}$$

where k_l is condensed liquid thermal conductivity.

Resistance due to the functional coating R_{fc} is defined as,

$$R_{fc} = \frac{h_{fc}}{\pi r^2 \sin^2\theta k_{fc}} \tag{17}$$

where h_{fc} and k_{fc} are thickness and thermal conductivity of the functional coating, respectively.

Total thermal resistances on a plain hydrophobic surface are $R_{total} = R_c + R_i + R_d + R_{fc}$

On superhydrophobic surface, for the Wentzel state conduction resistance due to the functional coating R_{fc} and structures R_{st}, and liquid bridge R_g, parallel resistance thermal circuit analysis is utilized. Other resistance parameters including R_c, R_i, and R_d is the same as thermal resistance analysis on the plain hydrophobic surface.

With the Wenzel wetting morphology, the conduction resistance due to the functional coating is,

$$R_{fc} = \frac{h_{fc}}{\psi \pi r^2 \sin^2\theta k_{fc}} \tag{18}$$

where Ψ is is the structured surface solid fraction.

and the conduction resistance by structures is,

$$R_{st} = \frac{h_{st}}{\psi \pi r^2 \sin^2 \theta \, k_{st}} \tag{19}$$

where h_{st} and k_{st} are thickness and thermal conductivity of the functional coating, respectively. Total thermal resistances on a structured superhydrophobic surface becomes,

Resistance due to the liquid bridge

$$R_g = \frac{h_g}{(1-\psi) \pi r^2 \sin^2 \theta \, k_l} \tag{20}$$

where h_g and k_l are thickness and thermal conductivity of the condensed droplet, respectively. Total thermal resistances on a plain hydrophobic surface is

$$R_{total} = R_c + R_i + R_d + R_{parallel} \tag{21}$$

where $R_{paralle}$ is defined as,

$$R_{parallel} = \left(\underbrace{\frac{1}{R_g + R_{fc}}}_{1-\Psi} + \underbrace{\frac{1}{R_{st} + R_{fc}}}_{\Psi} \right)^{-1} = \left[\frac{1}{\frac{h_g}{(1-\psi)\pi r^2 \sin^2 \theta \, k_l} + \frac{h_{fc}}{(1-\psi)\pi r^2 \sin^2 \theta \, k_{fc}}} + \frac{1}{\frac{h_{st}}{\psi \pi r^2 \sin^2 \theta \, k_{st}} + \frac{h_{fc}}{\psi \pi r^2 \sin^2 \theta \, k_{fc}}} \right]^{-1} =$$

$$= \frac{1}{\pi r^2 \sin^2 \theta \, k_{fc}} \left[\frac{(1-\psi)k_l}{h_g k_{fc} + h_{fc} k_l} + \frac{\psi k_{st}}{h_{st} k_{fc} + h_{fc} k_{st}} \right]^{-1} \tag{22}$$

3 COPPER-BASED SUPERHYDROPHOBIC NANOSTRUCTURES FOR HEAT TRANSFER IN FLOW CONDENSATION

3.1 Objective of the Study

In this study, we experimentally investigated flow condensation heat transfer enhancement in a minichannel with a nanostructured superhydrophobic surface in a wide range of steam mass fluxes, different steam inlet qualities, and cooling water mass flow rates. We elaborated more on visualization by investigating visual droplet dynamics such as the percentage of droplet diameter distribution at different time frames of a condensation cycle, droplet departure diameters, cycle time, and droplet number density. We demonstrated that beside high vapor shear stress exerted by the flow on the interface of vapor and condensed liquid, we can take advantage of an inherently

unique water repellency feature of superhydrophobic surfaces in flow condensation for enhancing the condensation heat transfer performance.

3.2   Sample Preparation and Characterization

Copper alloy (99% purity) substrates with dimensions of $0.5 \times 10 \times 37$ (mm³) were used as the substrates. Acetone, isopropyl alcohol, deionized (DI) water, and 2 M solution of hydrochloric acid (Sigma-Aldrich, 36%) were utilized in order to clean and prepare the copper surfaces for surface treatment. Sodium hydroxide (NaOH, Merck) and ammonium persulfate (($NH_4)_2S_2O_8$, neoFroxx) were employed to prepare a mixture for wet etching of the substrates. An ethanol (99.9% purity) solution of 1H,1H,2H,2H-Perfluorodecanethiol, PFDT, (Sigma-Aldrich) was used to reduce the surface energy of the substrates.

First, the samples were polished with sandpaper for a mirrorlike finish, followed by cleaning by acetone in an ultrasonic bath for 10 min and rinsing with isopropyl alcohol and DI water. To remove the native oxide film, the samples were dipped in a 2 M solution of HCl for 10 min, then rinsed with DI water, and dried with nitrogen gun. Superhydrophobic surfaces were fabricated using wet chemical etching [82].
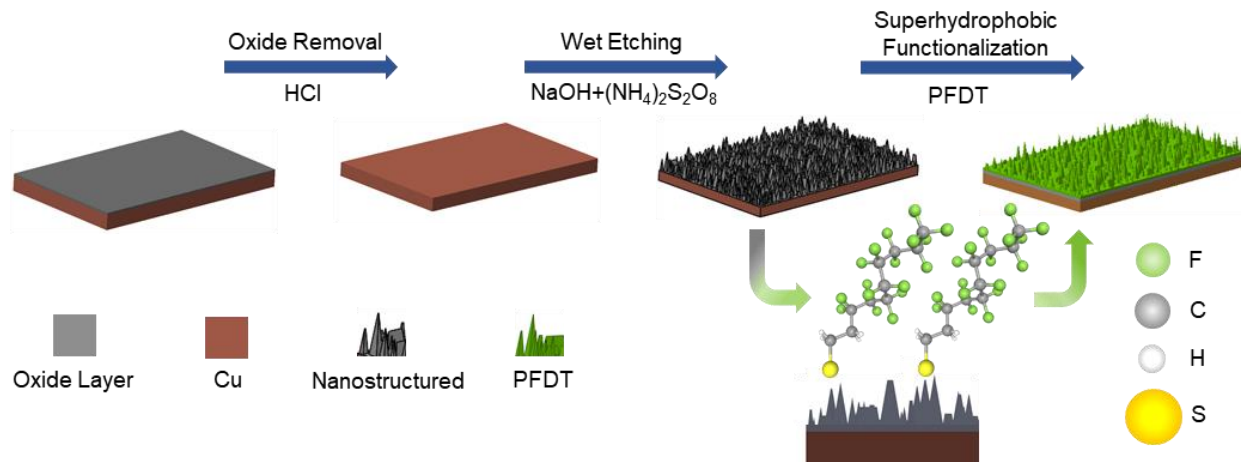
Figure 6. Illustration of the fabrication of the copper-based nanostructured superhydrophobic surface

After removing the native oxide film, a two-step process was adopted to prepare the superhydrophobic surfaces as shown in **Figure 6**. In the first step, the polished and cleaned copper samples were immersed for 30 min in a mixture solution of 2.5 M NaOH and O.1 M ($NH_4)_2S_2O_8$, which was stirred continuously to ensure the uniformity in nanostructure formation on the

substrates. Afterwards, the samples were rinsed in DI water and dried with nitrogen gas. These processes made the samples have superhydrophilic nature with contact angles of about 4°. The second step was to reduce the surface energy of nanostructured surface using an ethanol solution of 1H,1H,2H,2H-Perfluorodecanethiol (volume ratio: 100:1). The samples were immersed in the solution for 2 h, followed by washing with pure ethanol for 1 h, and drying with nitrogen stream. This step dramatically reduced the surface energy of surfaces, resulting in a contact angle of around 171°. Except skipping the chemical etching step, the same surface modification processes were used for the preparation of hydrophobic surfaces. The hydrophobic surfaces had a contact angle of about 116°.

Water contact angle measurements and Scanning Electron Microscopy (SEM) techniques were used to characterize the surfaces. **Figure 7**a and b illustrate the SEM images of flake shaped nanostructures, which promote nucleation of the droplets. Attension® Theta Lite optical tensiometer was used to measure the contact angle of the surfaces. 5 μL water droplets were placed on different locations of the surface. Six sessile contact angle measurements were performed on one surface, and the results were averaged. Contact angles of the bare mirror-finish copper, superhydrophilic copper, hydrophobic copper, and superhydrophobic copper surfaces are shown in and **Figure 8** a, b, c, and d, respectively.
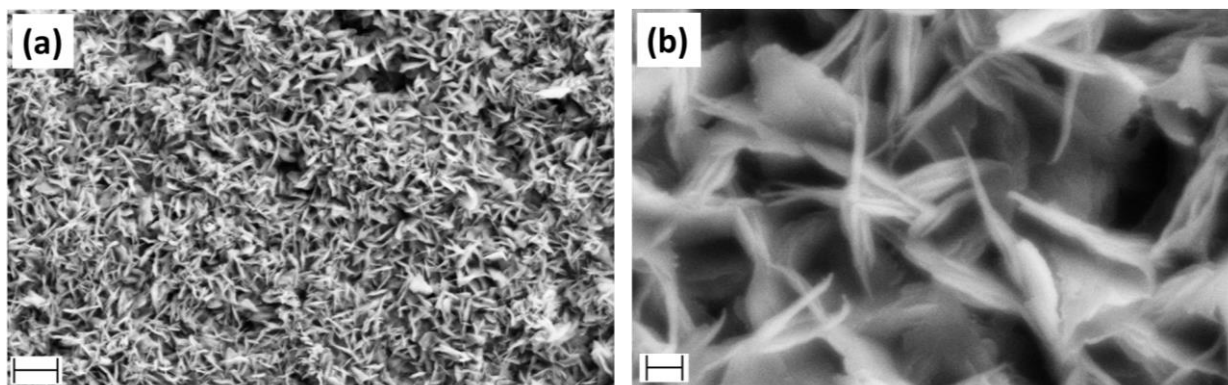
Figure 7. Characterization of the nanostructured surface. (a) Scanning electron microscope (SEM) images of nanostructured surface; scale bar is 2 mm. (b) SEM image with high magnification, which shows the detailed flake shape of the nanostructures; scale bar is 200 nm.
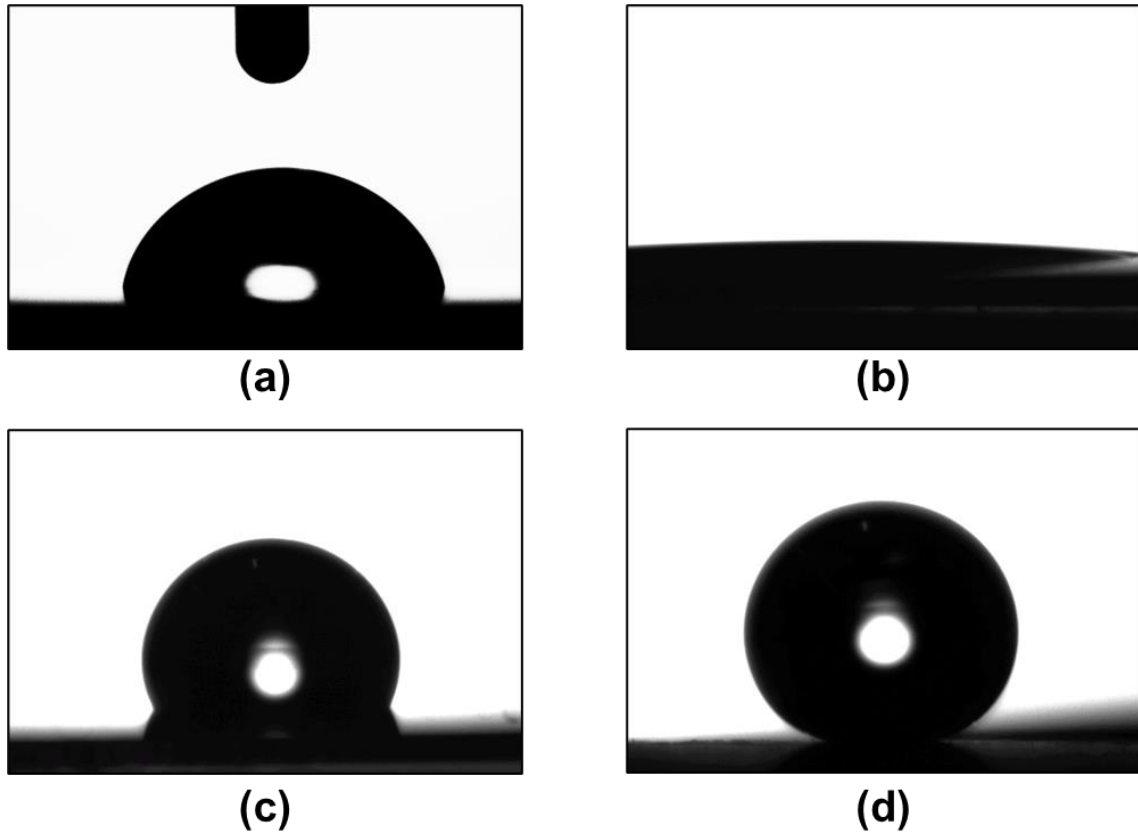
Figure 8. Sessile water droplets on: (a) bare mirror-finish copper, (b) superhydrophilic copper, (c) hydrophobic copper, and (d) superhydrophobic copper surfaces

The Contact angles measurements for all the samples are displayed in **Table 2**.

Table 2. Contact angles for different copper surfaces before and after treatments.

Surface	Contact angle
Bare mirror-finish copper	$78 \pm 1°$
Superhydrophilic copper	$4 \pm 1°$
Hydrophobic copper	$116 \pm 2°$
Superhydrophobic copper	$171 \pm 3°$

3.3   Image Analysis

Visualization studies were simultaneously performed using the high-speed camera system. Real-time images of dropwise condensation were captured with the sampling rate of 2000 frames

per second and the resolution of 128×128 pixels. In-house MATLAB scripts were developed to analyze the recorded images (see the Supporting Information for further details).

An in-house MATLAB code (MATLAB^{TM} 2018a, MathWorks, Inc., Natick, MA) was developed to detect the droplets on each frame and measure their size over a condensation cycle (Figure 9). The sampling speed during visualization was 2000 frame per second. For droplet size distribution, each condensation cycle was divided into 5 time-intervals: 0-$\tau/5$, $\tau/5$-$2\tau/5$, $2\tau/5$-$3\tau/5$, $3\tau/5$-$4\tau/5$, and $4\tau/5$-τ (τ is the duration of each condensation cycle). 100 frames were selected from each time interval with equal time differences, and the number and size of droplets were determined in each frame using the developed MATLAB code. Having the number of droplets for each size interval (e.g. 50-100 μm) on a frame, the time-averaged number of droplets for each size-interval was obtained by averaging the number of droplets on 100 frames. This averaging process was repeated for each time interval. 5 Different dropwise condensation cycle was selected for each steam mass flux and after repeating the whole process for each cycle, the results were averaged to reduce the error of the employed image processing method. **Figure 10**, shows five typical processed images for the superhydrophobic surface at the end of each time interval for steam mass flux of 10 kg/m^{2}s and cooling flowrate of 9.11 g/s. In the first frame, which is the beginning of dropwise condensation cycle, droplets start to nucleate. In the second and third frame, the nucleated droplets start to grow. When droplets get larger, they start to coalesce into larger droplets and at tend to leave the surface as a result of vapor shear force at the end of cycle[61] (The last frame in **Figure 10**, The whole process was performed for other steam mass fluxes as well.
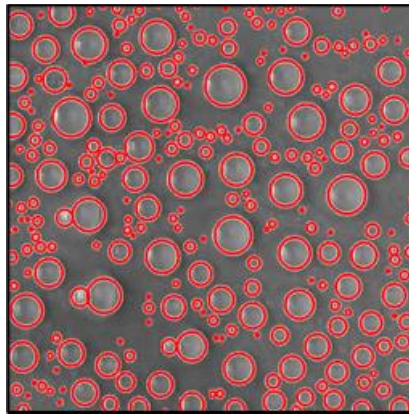
Figure 9. Droplet detection on the captured frames using the developed MATLAB code.

| t=121.5 ms (τ/5) | t=243 ms (2τ/5) | t=364.5 ms (3τ/5) | t=486 ms (4τ/5) | t=607.5 ms (τ) |
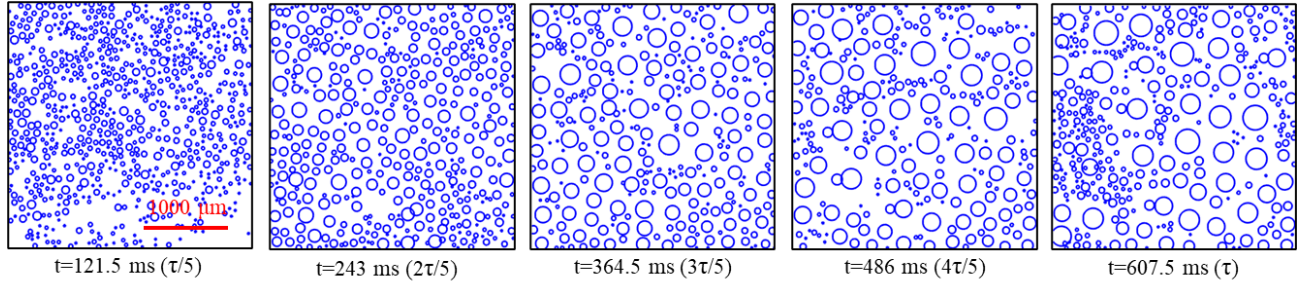
Figure 10. Five typical processed frames of dropwise condensation over one cycle (from nucleation to exactly before droplet departure). The above frames are for steam mass flux of 10 kg/m2s, cooling flowrate of 9.11 g/s, and for superhydrophobic surface.
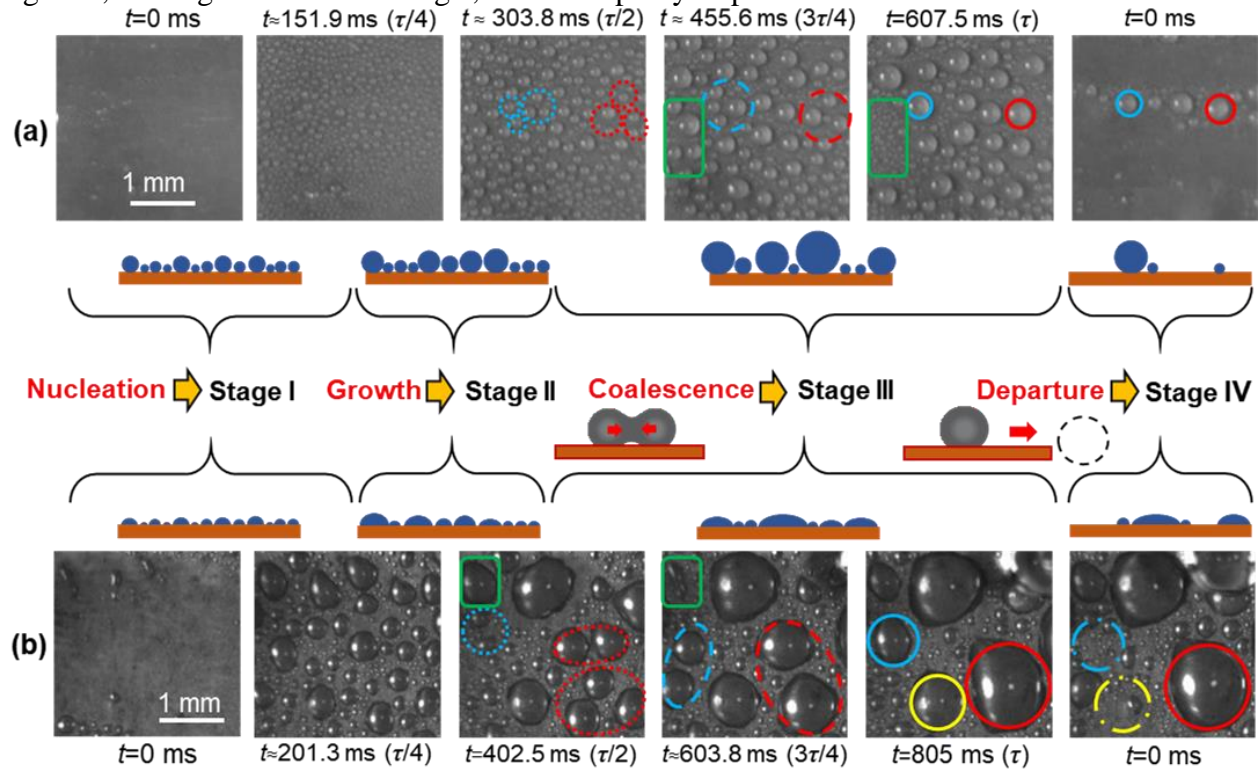
Figure 11. Full cycle of dropwise condensation for steam mass flux of G_s=10 kg/m^{2}s and cooling water mass flow rate of m_{cw}=9.11 g/s on (a) Superhydrophobic surface, and (b) Hydrophobic surface.

3.4   Results and Discussion

3.4.1   Visualization Study of Dropwise Condensation

In this section, the real time images captured by the high-speed camera were used to investigate the droplet dynamics at different stages of dropwise condensation. For both hydrophobic and

23

superhydrophobic surfaces, the effect of steam mass flux on cycle time and droplet size distribution was studied.

Condensation cycle, defined as the sequence of droplet nucleation, growth and departure, is a useful tool to characterize the condensation phenomenon. To compare the dropwise condensation performance of the fabricated hydrophobic and superhydrophobic surfaces, condensation cycles consisting of nucleation (stage I), growth (stage II), coalescence (stage III), and departure (stage IV) are shown in **Figure 11.** In the analysis, τ stands for the full cycle period.

Figure 11 shows a full cycle of dropwise condensation for the superhydrophobic surface at steam mass flux of 10 kg/m2s and cooling water mass flowrate of 9.11 g/s. At stage I, the droplets start to nucleate. The droplet nucleation rate depends on several parameters including the surface wettability and temperature, vapor hydrothermal properties, and the content of non-condensable gas in the vapor flow. It should be noted that the beginning of this stage corresponds to the end of previous cycle, where sweeping large droplets leave the surface. As can be seen in the second and third frames, over time, the droplets start to grow as a result of continuous vapor condensation (stage II). At stage III, droplets start to merge and form larger droplets. The blue and red circles in **Figure 11**a display how the adjacent droplets coalesce into larger droplets in the next frames. At stage IV, as shown in the last frame, the droplets start to sweep and make room for the nucleation in the following cycle.

The full cycle of dropwise condensation under the same experimental conditions is shown in **Figure 11**b for the hydrophobic surface. Similar to the superhydrophobic surface, small droplets start to nucleate at t=0. The droplet size distribution at $\tau/4$ indicates that the droplets tend to coalesce quicker on the hydrophobic surface compared to the superhydrophobic surface, which leads to larger droplets on the hydrophobic surface. On the other hand, the superhydrophobic surface provides a more uniform droplet size distribution (compare **Figure 11**a and b). The spreading movement of large droplets on the hydrophobic surface acts as a thermal resistance and has a negative effect on the heat transfer performance.
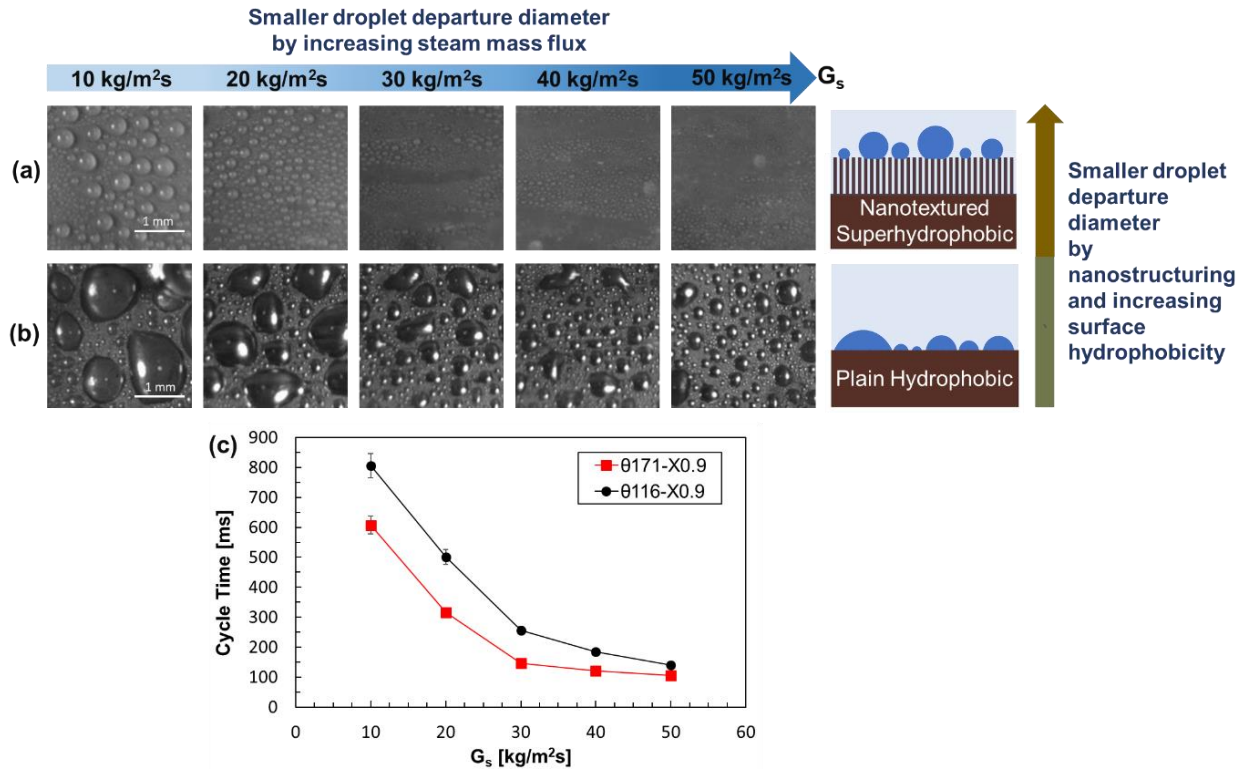
Figure 12. Droplet distribution at the end of a dropwise condensation cycle at various steam mass fluxes for the (a) superhydrophobic and (b) hydrophobic surface. (c) Condensation cycle duration change at different steam mass fluxes.

On the superhydrophobic surface, after the first droplet departure, depending on steam mass flux, it takes about 20-200 ms before all the droplets in the frame leave the surface. Some droplets leave the surface a few milliseconds later than the first droplet departure, because the resistant forces are higher so that higher shear rates for droplet detachment are required. In this study, the departure time of the first droplet was considered to be the end of the cycle. As can be seen in **Figure 11**a, for the superhydrophobic surface, most of the droplets leave the surface at the end of cycle. However, for the hydrophobic surface (**Figure 11**b), there are still droplets attached to the surface. Unlike the superhydrophobic surface, the droplet departure time varies noticeably for different droplets on the hydrophobic surface. As can be seen in the last frame of **Figure 11**b, while two large droplets have left the surface by shear force (blue and yellow circles), some droplets (red circle) remained attached to the surface. The droplets, which are attached to the surface, continue growing to a larger size so that they can depart as a result of vapor shear force, while new droplets start to form on the opened areas for the new cycle.

Although droplets grow faster on the hydrophobic surface, it has a longer cycle duration compared to the superhydrophobic surface (τ_{phob}=805 ms vs. τ_{sup}=607.5 ms). Due to the higher surface wettability, the droplets at the end of the cycle are considerably larger on the hydrophobic surface. The droplets tend to continue growing on the hydrophobic surface until the vapor shear rate is large enough to detach the droplets from the surface[76]. Although detachment of larger droplets from the surface is more likely to occur, some detachments of smaller droplets occur on both hydrophobic and superhydrophobic surfaces (as shown by green color in Figure 11), which is the result of coalescence between two adjacent droplets. Due to the released surface energy, some smaller droplets (compared to the droplet diameter at the end of cycle) could gain enough mobility to leave the surface because of vapor shear rate.

Figure 12 shows the droplet distributions on the superhydrophobic and hydrophobic surfaces at the end of condensation cycle for various steam mass fluxes. The vapor shear rate increases with steam mass flux, resulting in faster departure of the droplets from the surface. As can be seen in Figure 12a, the size of the departing droplets at the end of condensation cycle is remarkably reduced when the steam flux increases from 10 to 20 kg/m²s. The difference is even notable when the steam mass flux reaches 30 kg/m²s. Beyond this mass flux (40 and 50 kg/m²s), the reduction in droplet departure size with steam mass flux increase disappears (refer to Video S1 and Video S2 for more information). This trend is also similar for the hydrophobic surface (**Figure 12b**). Although the vapor shear rate is greater on the hydrophobic surface because of larger droplet sizes, the higher surface energy of this surface makes it harder for droplets to become detached. Figure 12c shows the effect of steam mass flux on the condensation cycle duration. An increase in steam mass flux from 10 to 30 kg/m²s reduces the droplet departure time from 607.5 to 316 ms for the superhydrophobic surface and from 805 to 500 ms for the hydrophobic surface, respectively. Nonetheless, the rate of reduction in the duration becomes lower beyond the steam mass flux of 30 kg/m²s. For both superhydrophobic and hydrophobic surfaces, increasing the mass flux from 10 to 30 kg/m²s results in a noticeable increase in the drag force, which leads to much quicker departure of the droplets. However, when increasing the mass flux to 40 and then to 50 kg/m²s, the exerted drag force grows with a lower rate, and there is only a small change in cycle duration (A simplified approach regarding the relation between drag force and droplet departure diameter could be found in section 3.3). Quicker departure of droplets with smaller diameters lowers the

condensate thermal resistance and leads to a better heat transfer performance at higher steam mass fluxes.
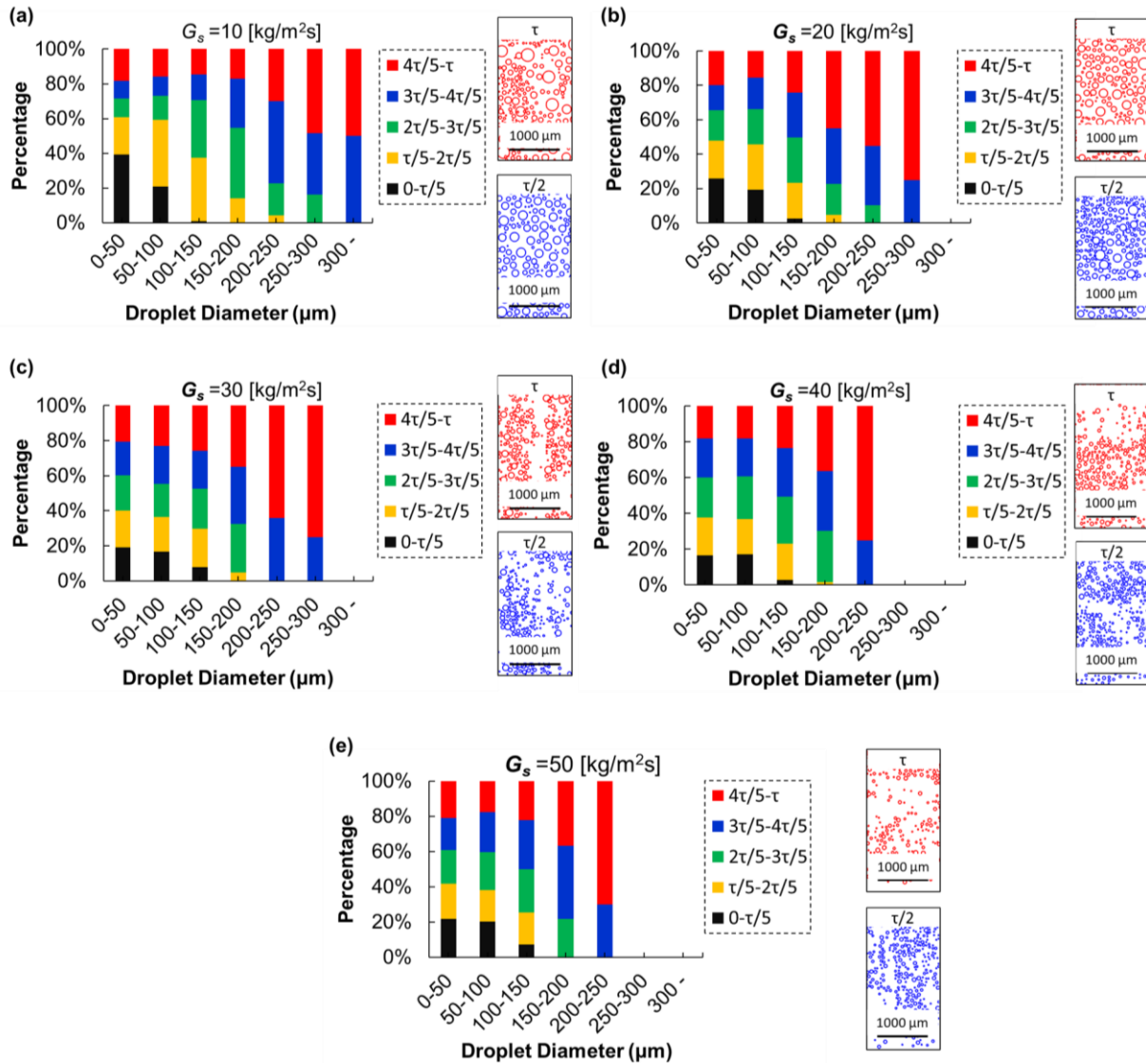
Figure 13. Time-averaged histogram of droplet diameters for the superhydrophobic surface at different steam mass fluxes, for steam mass flux G_s of (a) 10, (b) 20, (c) 30, (d) 40, and (e) 50 kg/m^{2}s (τ is the cycle duration).
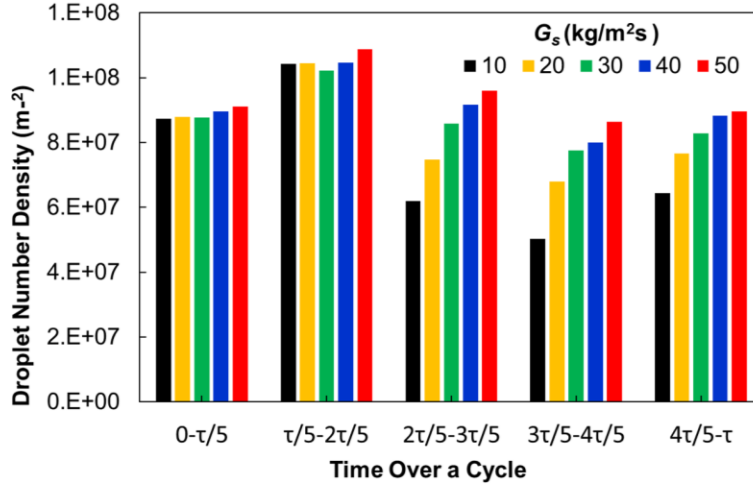
Figure 14. Time-averaged droplet number density on the superhydrophobic surface for various steam mass fluxes of G_s=10-50 kg/m²s (τ is the cycle duration).

Droplet distribution data were further analyzed and reduced so that droplet diameter histograms over condensation cycles are prepared for the superhydrophobic surface (Figure 13) (section S5 for details). Accordingly, for steam mass flux of 10 kg/m²s, the percentage of small droplets on the surface (0-50 μm) is 39% at the first interval of condensation cycle. This percentage decreases over the cycle until the fourth interval, where it reaches 10%. After the nucleation and growth stages, droplets start to coalesce and form larger droplets, which in turn reduces the number of small droplets. By the end of the cycle, droplets reach their largest size, thereby leading to vacant places for new nucleation in the next condensation cycle (Figure 11). As a result, the percentage of droplets with the size range of 0-50 μm slightly increases at the end of cycles for all the steam mass fluxes.

An increase in steam mass flux results in a better distribution of 0-50 μm droplets over the entire cycle, which is advantageous in terms of condensation heat transfer. As can be seen in Figure 13, while the size of droplets reaches over 300 μm at the end of the condensation cycle for the mass flux of 10 kg/m²s, for steam mass fluxes of 20 and 30 kg/m²s there are no droplets larger than 300 μm anymore. For the mass fluxes of 40 and 50 kg/m²s the largest droplets were smaller than 250 μm. This explains the effect of mass flux on condensate thermal resistance reduction. As a result, heat transfer coefficient increases with steam mass flux for all the samples. Furthermore, the results reveal that for mass fluxes higher than 20 kg/m²s, the droplets with diameters smaller than 100 μm are almost equally distributed over the whole condensation cycle, which is highly effective in improving convective heat transfer during dropwise condensation.

28

The droplet number density on the superhydrophobic surface for various steam mass fluxes is shown in Figure 14. At the start of the cycle, the droplet number density is almost the same for all the mass fluxes. However, a major difference in the number density between different steam mass fluxes lies after the third interval. As discussed earlier, the vapor shear force is not sufficient to detach the droplets from the surface at smaller mass fluxes. Therefore, a considerable part of the surface is filled with large droplets, which provides only a limited space for nucleation.
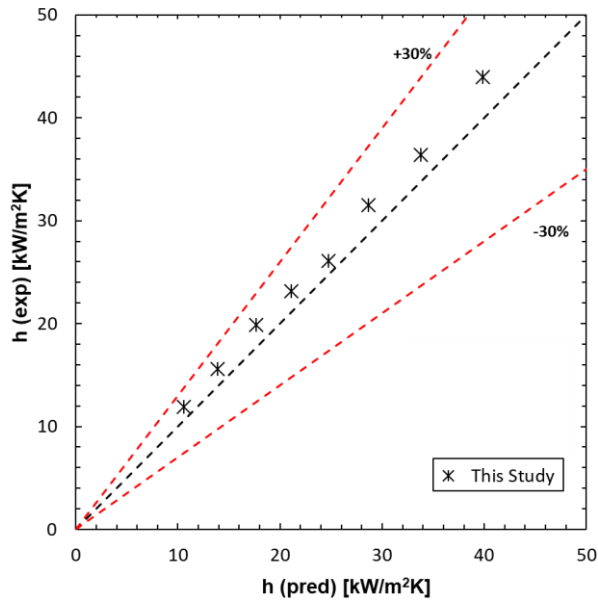
Figure 15. Experimental heat transfer coefficients (hydrophilic surface) predicted by the correlation of Kim and Mudawar[83] for validation
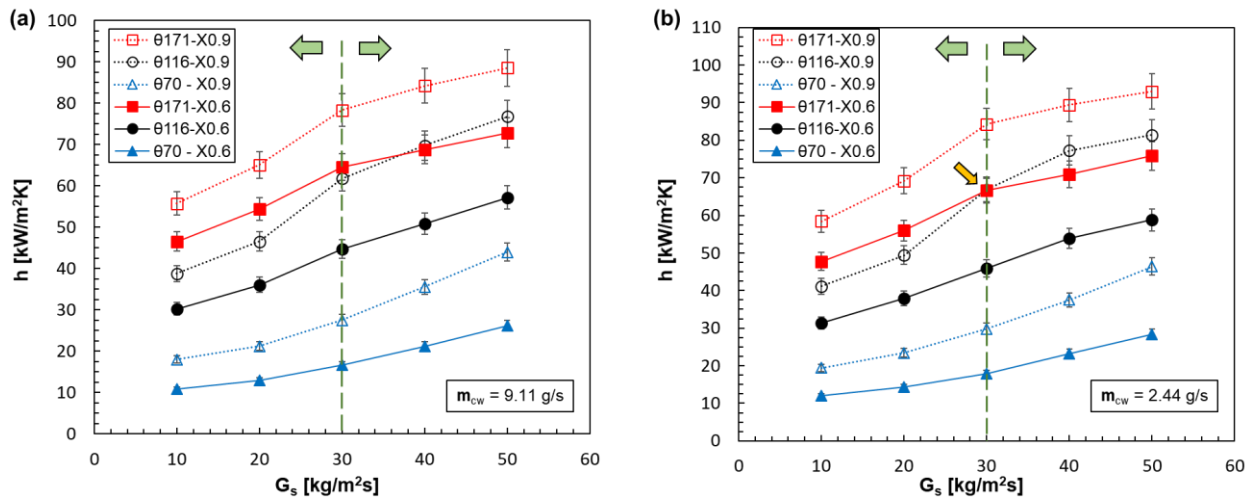
Figure 16. Heat transfer coefficient (h) as a function of steam mass flux (G_s) with inlet qualities of $X=0.6$ (X0.6) and $X=0.9$ (X0.9) for three test surfaces: nanostructured superhydrophobic

(θ171), plain hydrophobic (θ116), and hydrophilic (θ70). Cooling water mass flow rates (a) m_{cw} = 9.11 g/s and (b) m_{cw} = 2.44 g/s

3.4.2   Heat Transfer Analysis

This section focuses on the effect of steam mass flux, inlet steam quality and cooling water mass flow rate on heat transfer coefficients. In addition, the overall effect of average steam quality on heat transfer coefficient of superhydrophobic, hydrophobic, and hydrophilic surfaces were examined.

To validate the experimental setup and the adopted approach, the obtained heat transfer coefficients for filmwise condensation on the hydrophilic surface were compared with the predictions of the Kim and Mudawar's correlation[83], which was developed for filmwise condensation and pre-dominantly annular flow regimes. The equation 3, which utilizes the two-phase multiplier approach[84] and modified Weber number[85], is based on the consolidated heat transfer coefficient data points from the literature with single and multichannel configurations for various working fluids, vapor qualities (from 0-1), and mass fluxes (in the range of 53 to 1403 kg/m²s).

$$h_{pred} = \frac{k_f}{D_h} 0.048 Re_f^{0.69} Pr_f^{0.34} \frac{\phi_g}{X_{tt}} \tag{3}$$

More detailed explanation about the parameters included in the correlation could be found in the study of Kim and Mudawar[83,86].

To assess the prediction capability of the correlation, the mean absolute error (MAE), which is defined as, is utilized:

$$MAE = \frac{1}{M} \sum_{i=1}^{M} \frac{|h_{pred} - h_{exp}|}{h_{exp}} \times 100\% \tag{4}$$

Here, h_{pred} and h_{exp} are predicted and measured experimental heat transfer coefficient values, respectively. Figure 15 shows the predictions of the correlation. As can be seen, the experimental results are in a good agreement with the predictions of the correlation (with mean absolute error MAE of 9.1%).

Figure 16 shows the heat transfer coefficient as a function of steam mass flux for three surfaces and different inlet qualities, and coolant mass flow rates. As can be seen, very high heat transfer

coefficients (maximum value of $h \approx 93$ kW/m^{2}K) can be achieved with superhydrophobic surfaces. Although heat transfer coefficients for all surfaces increases with steam mass flux, the rate of enhancement strongly depends on the surface properties and inlet steam quality. On the superhydrophobic surface, at the inlet quality of 0.9, an increase in mass flux from 10 kg/m^{2}s to 30 kg/m^{2}s results in the average enhancement of 18%. On the other hand, when the mass flux increases from 30 kg/m^{2}s to 50 kg/m^{2}s, only a 6% stepwise increase in heat transfer coefficients can be obtained. A similar trend in heat transfer coefficient is observed for the hydrophobic surface at the inlet quality of 0.9. Although the maximum increase in heat transfer coefficient with steam mass flux on the superhydrophobic surface is 59%, the hydrophobic surface demonstrates a 98% increase in the thermal performance. This shows that the hydrophobic surface is more sensitive to the steam mass flux compared to the superhydrophobic surface. The hydrophilic surface exhibits a stronger dependence on the steam mass flux such that the overall heat transfer increase is 144%, which is larger than both hydrophobic and superhydrophobic surfaces.

Heat transfer enhancement with steam flow is due to the exerted shear force on the interface of vapor and condensed liquid. During condensation, the condensate acts as thermal resistance between the flowing steam and cooling surface. On hydrophilic surfaces, film condensation can be observed, and heat transfer enhancement with mass flux is due to the decrease in liquid film thickness. Interfacial shear force increases with steam mass flux and results in liquid film thickness decrease. On the hydrophobic and superhydrophobic surfaces, which trigger dropwise condensation, heat transfer enhancement with steam mass flux is due to the increase in droplet mobility. An increase in mass flux not only limits the droplet departure diameter but also reduces the condensation cycle time.

The experimental results (Figure 16) highlight that a larger portion of the surface is filled with small size droplets with mass flux. Since small size droplets have a lower thermal resistance compared to the larger ones, the increase in the number of smaller droplets improves the heat transfer performance of the superhydrophobic surface. Furthermore, at the same mass flux, the decrease in condensation cycle time corresponding to the superhydrophobic surface compared to hydrophobic surface (Figure 12c) causes an increase in the droplet nucleation process. Enhanced condensation heat transfer for nanostructured superhydrophobic surface compared to the plain hydrophobic surface is attributed to the combined effect of droplet departure size decrease, increased number of smaller droplets, and cycle time reduction.

As shown in Figure 16, although heat transfer coefficient increases with vapor quality for all the samples, the hydrophobic surface exhibits a stronger dependency on vapor quality compared to the superhydrophobic surface. The superhydrophobic surface demonstrates a similar increasing trend with vapor quality for all mass fluxes, where the heat transfer coefficient increase is 20%. However, the hydrophobic surface has a higher increase (33%) in heat transfer coefficient over the whole vapor quality range. The hydrophilic surface leads to an increase 65% over the whole quality range, which is the highest among the three surfaces.

The increase in condensation heat transfer coefficient with inlet steam quality is attributed to the liquid content of steam flow. For the hydrophilic surface, the heat transfer coefficient increases with steam quality as the liquid film becomes thinner. For hydrophobic and superhydrophobic surfaces, the increase in condensation heat transfer coefficient with inlet quality is due to the decrease in droplet departure diameter and reduction in cycle time. At both inlet qualities and the same steam mass flux, the heat transfer performance of the nanostructured superhydrophobic surface outperforms the plain hydrophobic surface. It can be therefore inferred that nanostructures on the superhydrophobic surface promote partial wetting state, where the droplets are more mobile compared to the hydrophobic surface.

Figure 16a, and Figure 16b display heat transfer coefficient as a function of steam mass flux with cooling water mass flow rates of 9.11g/s and 2.44 g/s, respectively. Condensation heat transfer coefficient slightly increases with the reduction in cooling water mass flow rate, and condensation heat transfer weakly depends on the cooling water mass flow rate. Heat flux increases with coolant mass flow rate, which is due to increased temperature difference between two thermocouple planes. In addition, this leads to higher surface subcooling because of the reduced surface temperature. As the driving force of condensation, an increase in surface subcooling, which is induced by enlarging the coolant mass flow rate in our experiments, enhances the droplet nucleation density and growth rate, which promotes the formation of large pinned droplets during dropwise condensation[55]. Large pinned droplets increase the cycle time and refreshing period, thereby causing a reduction in the heat transfer coefficient. On the other side, for the hydrophilic surface, a reduction in condensation heat transfer coefficient with further surface cooling is related to the increased liquid film thickness. Furthermore, outlet quality of the steam flow decreases with coolant mass flow rate. By the definition provided by Equation S.5, keeping all other parameters

constant, an increase in coolant mass flow rate enhances heat transfer, which reduces outlet quality of the steam flow.
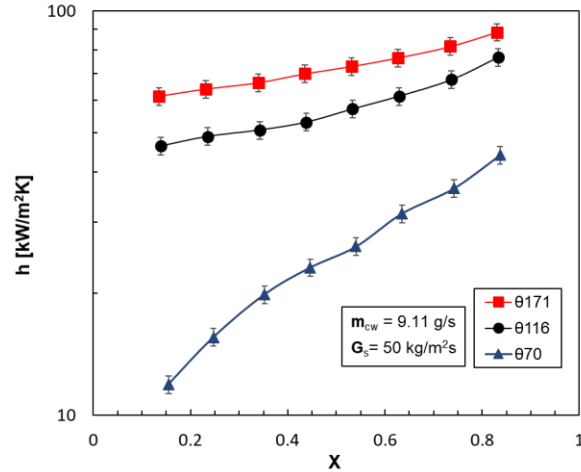
Figure 17. Heat transfer coefficient as a function of steam quality at steam mass flux of G_s= 50 kg/m^{2}s and cooling water mass flow rate of m_{cw} = 9.11 g/s for three test surfaces: nanostructured superhydrophobic (θ171), plain hydrophobic (θ116), and hydrophilic (θ70).

Figure 17 shows the variation in heat transfer coefficient with average steam quality, which is obtained by averaging the steam inlet and outlet quality. Condensation heat transfer coefficient increases with steam quality due to the decrease in liquid film thickness. The slope of heat transfer coefficient profile is considerably higher for the hydrophilic surfaces compared to the both hydrophobic and superhydrophobic surfaces. On the other side, during dropwise condensation, especially for the superhydrophobic surface, condensation heat transfer coefficient monotonically increases with steam quality. Relative to conventional dropwise condensation on the plain hydrophobic surface, the superhydrophobic surface offers up to 33% enhancement in heat transfer.

At lower steam qualities, high saturated liquid content of the steam flow acts as a barrier to condensation. For the hydrophilic surface, the liquid film on the surface becomes thicker with a decrease in the steam quality. While saturated liquid and highly pinned condensed droplets wet the hydrophobic surface at lower qualities, the superhydrophobic surface promotes condensation by repelling saturated liquid present in the flow from the surface allowing the formation of new condensed droplets on the surface.
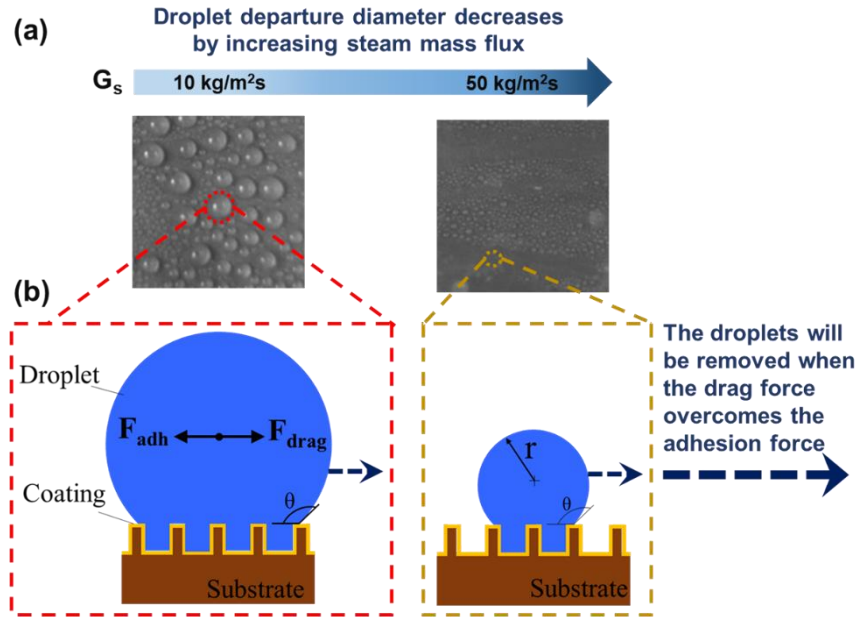
Figure 18. Droplet departure mechanism because of vapor drag. a) Real time images of condensation for mass fluxes of 10 and 50 kg/m²s. b) Schematic of the forces acting on the droplet on the nanostructured superhydrophobic surface during flow condensation. The droplet departure diameter decreases with steam mass flux due to the increased vapor velocity. The droplets will be removed when the drag force, which increases with steam mass flux, overcomes the adhesion force.

3.4.3 Steam Flow Condensation Mechanisms on Nanostructured Superhydrophobic Surface

According to Young[87], on a smooth surface with high surface energy droplets can wet or be spread on the surface. On the other side, on a rough surface, a liquid droplet might show Wenzel state [88] by penetrating into the cavities, or in the Cassie-Baxter state [89], where air is trapped in the cavities[90]. When measuring the contact angle of a superhydrophobic surface under the atmospheric condition, the trapped air under the droplets could lead to the Cassie-Baxter state. However, during flow condensation experiments, the nucleation of droplets takes place within nanostructures, because the concentration of non-condensable gases in the flow system is minimized[91]. This behavior leads to the formation of highly pinned droplets as shown in the visualization study (refer to Video S1 and S2). Therefore, in our experiments, the droplets tend to offer the Wenzel state, leading to lower mobility of the droplets compared to the Cassie-Baxter state.

According to Volmer's nucleation theory[92] , for nucleation of liquid droplets on a surface, minimum energy barrier ΔG should be overcome:

$$\Delta G = \frac{\pi r_{\min}^2 \sigma \left(2 - 3\cos\theta + \cos^3\theta\right)}{3} \qquad (5)$$

where θ is the contact angle and r_{min} is minimum nucleation radius defined as:

$$r_{\min} = \frac{2\sigma T_{sat}}{\rho_l h_{fg} \Delta T} \qquad (6)$$

where ρ_l, h_{fg}, and ΔT are the liquid density, latent heat of phase change, and temperature difference between vapor and condensing surface. It is evident that free energy barrier strongly depends on the contact angle of the condensing surface such that the nucleation process on hydrophilic surface requires less energy barrier to overcome compared to hydrophobic/superhydrophobic surfaces. In our study, when the contact angle is increased from 116° (hydrophobic) to 171° (superhydrophobic), ΔG increases by 23.8%. This explains the reason why droplet nucleation growth and coalescence process occur easier and faster on the hydrophobic surface compared to the superhydrophobic surface (see Figure 11 Figure 12 and Video S1-S4).

On hydrophobic and superhydrophobic surfaces, nucleated droplets start to grow by direct vapor-liquid condensation. For tilted or vertically oriented surfaces, growing droplets coalesce with neighboring droplets, and continue growing until they depart from the surface because of the gravitational force acting on them. However, unlike gravity-driven droplet departure, droplet removal in flow condensation is governed by two opposing forces of flow-droplet shear force (in the flow direction) and droplet-substrate adhesion force (in the opposite direction). Droplets are removed from the surface because of the vapor shear stress force acting on the interface of the condensed droplet. Neglecting the effect of gravity, the forces acting on a single droplet during flow condensation are the vapor drag force F_{drag} and adhesion force F_{adh}, as shown in Figure 18. It should be noted that the force analysis on droplets in confined channels is a complex process, and the proposed analysis is provided to give an understanding on the physics of the droplet departure process. For a droplet to depart from the surface, the adhesion force must be overcome by the drag force of the vapor flow[93].

The adhesion force acting on a liquid droplet with any shape is expressed by Antonini et al.[94] as:

$$F_{adh} = -\sigma \int_0^L \cos\theta(l)\cos\psi(l) \qquad (7)$$

where L is the length of the contact line. The distribution of the contact angle along the contact line and distribution of the normal along the contact line are denoted as $\theta(l)$ and $\Psi(l)$, respectively.

The determinations of $\theta(l)$ and $\Psi(l)$ can be very complicated because of irregular shape of the droplets. Instead, to address the complexity of the functions $\theta(l)$ and $\Psi(l)$, Amirfazli et al.[93] introduced a parameter k. This parameter, beside accounting for contact angle distribution, considers irregular and deformed shapes of the liquid droplet. Equation 7 can be then reduced to a simplified model:

$$F_{adh} = k\sigma\left(\cos\theta_{max} - \cos\theta_{min}\right)L_b \qquad (8)$$

where the term $(\cos\theta_{max} - \cos\theta_{min})$ is the contact angle hysteresis and L_b is the length of the drop base. If we assume that the droplet is hemispherical in shape, the length of the drop base becomes the diameter of the droplet, $L_b = D$.

The interfacial drag force acting on the liquid droplet is the combination of skin and pressure drag:

$$F_{drag} = \frac{1}{2}\rho_v U_v^2 A C_D \qquad (9)$$

where ρ_v, and U_v are vapor density and velocity, respectively. C_D is the drag coefficient, which depends on contact angle and shape of the droplet. The frontal area of the droplet A can be accepted as $\pi D^2/8$ assuming that droplet is a hemisphere.

As mentioned above, for the droplet removal, the adhesion force must be overcome by vapor drag. Therefore, equating and rearranging Equation 9, the critical steam velocity U_{cr}, which is the velocity needed for the commencement of the droplet departure, can be obtained as:

$$U_{cr} = \sqrt{\frac{2k\sigma\left(\cos\theta_{max} - \cos\theta_{min}\right)L_b}{\rho_v A C_D}} = \sqrt{\frac{1}{D_{dep}}} \cdot S_c \qquad (10)$$

where S_c is a constant (if we assume that parameter k and C_D are constants[93]) depending on contact angle and shape of the droplet, and testing conditions. Note that in the equation 10, assuming hemispherical droplet, the $L_b = D_{dep}$ (D_{dep} being droplet departure diameter) and $A = \pi(D_{dep})^2/8$ is considered. Equation 10 clearly reveals that the droplet departure diameter decreases with steam velocity, which is in good agreement with the experimental data obtained in this study.

4 BIPHILIC SURFACES WITH OPTIMUM HYDROPHOBIC ISLANDS ON SUPERHYDROPHOBIC BACKGROUND FOR DROPWISE FLOW CONDENSATION

4.1 Objective of the Study

Here, we experimentally studied flow condensation heat transfer on biphilic surfaces in a minichannel with different steam mass flux. The biphilic surfaces are fabricated by obtaining circular hydrophobic islands on a superhydrophobic background. Hydrophobic islands in the range of 100 to 900 μm in diameter were fabricated using the combination of wet etching, surface functionalization, and physical vapor deposition techniques. We showed that there is an optimum island diameter D of the hydrophobic islands on a superhydrophobic substrate as a function of steam mass flux, where heat transfer performance is maximum. Finally, by fitting the experimental data, a correlation for prediction the optimum island diameter of biphilic surfaces is provided as a function of steam mass flux for flow condensation heat transfer.

4.2 Surface Fabrication and Characterization

4.2.1 Surface Preparation

Biphilic surfaces (hydrophobic islands on superhydrophobic substrate) were fabricated through three processes of wet etching, functionalization, and electron beam physical vapor deposition (PVD).

High purity copper (99% purity) substrates with as length, width, and thickness of 37, 10, and 0.5 mm, respectively, were used as the base material to fabricate biphilic surfaces. Before starting with the main fabrication process, the samples were carefully cleaned. Then, a mirror-like finish was reached through coarse to extra fine sandpapers. Therafter, the samples were cleaned with acetone in an ultrasonic bath, followed by rinsing with isopropyl alcohol. Afterwards, the surfaces were thoroughly rinsed with DI water and dried with nitrogen stream. To remove the native oxide film, the samples were dipped in 2 M solution of HCl for 10 minutes followed by rinsing with DI water and drying with nitrogen stream.
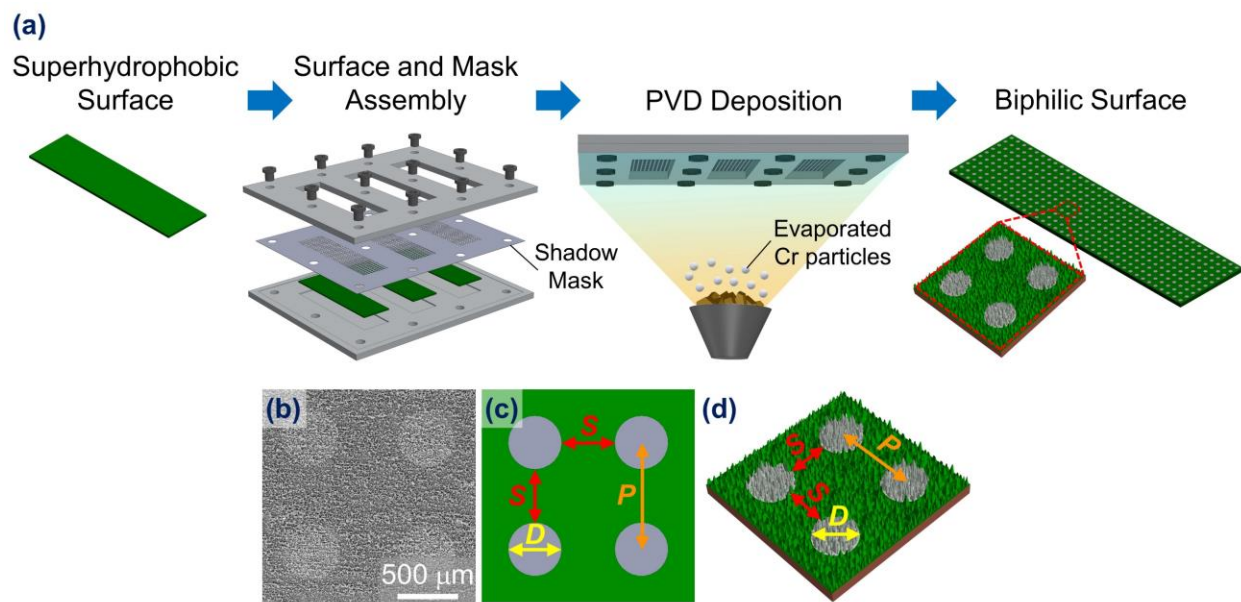
Figure 19. (a) Illustration of the fabrication steps of a nanostructured biphilic surface (hydrophobic islands on superhydrophobic substrate) by electron beam physical vapor deposition (PVD) technique. (b) SEM image of a biphilic surface with 500 μm islands. (c) Schematic of a biphilic surface. Hydrophobic islands (gray circular spots) are surrounded by superhydrophobic (green) areas. D is the diameter of hydrophobic islands; S is the edge-to-edge distance between the islands; P is the pitch size (center to center distance of the islands) which was kept constant (P=1 mm) for all the biphilic surfaces. (d) Magnified 3D view of a portion of the nanostructured biphilic surface.

The combination of wet etching and surface functionalization was utilized to obtain nanostructured superhydrophobic surface[82]. Nanostructured superhydrophobic surfaces were used as the base substrate to obtain biphilic patterns with hydrophobic islands. To fabricate nanostructured superhydrophobic substrates (without patterns), the method described in our previous study was adopted[95]. For this purpose, after polished and cleaning step, copper samples were immersed in a solution of 2.5 M NaOH and O.1 M $(NH_4)_2S_2O_8$ for 30 minutes to obtain nanostructured superhydrophilic surface with contact angles of 4°. After wet chemical etching process, the surface was functionalized using ethanol (99.9% purity) solution of 1H,1H,2H,2H-Perfluorodecanethiol (PFDT, Sigma-Aldrich) (volume ratio: 100:1) for 2 h. Subsequently, the surfaces were thoroughly washed in pure ethanol for 1 h. After surface functionalization, the surface energy of the surfaces was reduced, which resulted in superhydrophobic surfaces with a contact angle of about 172°.

Finally, the steps illustrated in **Figure 19**a, was followed to form circular hydrophobic islands on the nanostructure superhydrophobic substrate using the Electron Beam Physical Vapor deposition (PVD) technique. First, the desired patterns (circular islands with different diameter for each surface) were designed in a CAD software. Then, using computer-controlled laser, the designed patterns for each surface were transferred into a 0.2 mm thick stainless-steel. This step served for obtaining stainless-steel shadow masks required for patterning the superhydrophobic substrate. (See Section S1 of the Supporting Information for the shadow mask). Next, using the Electron Beam Physical Vapor Deposition (PVD) technique a 150 nm layer of Chromium was coated on the patterned regions. For this purpose, the surface, mask and mask holder were assembled and placed in a Torr International, Inc. E-beam evaporator. Chromium was used as the target material. Deposition rate of 2 Å/s was adopted to coat the 150 nm Chromium on the patterned regions. During the deposition process, the pressure of the chamber was $\sim 5 \times 10^{-6}$ mTorr. It worth to mention that the fabrication of biphilic surfaces with the method described above is facile and scalable (See **Figure 19**c and d, for the detailed illustration of geometrical configuration of a biphilic sample). As seen in Table 3, regarding hydrophobic islands, *D* and *S* are diameter and edge-to-edge distance between the hydrophobic islands, respectively. *P* is the pitch size (center to center distance of the islands), which was kept constant (*P*=1 mm) for all the biphilic surfaces.

Table 3. Geometric properties of the tested samples

Sample name	Island diameter D (μm)	Edge-to-Edge distance between islands S (μm)	Hydrophobic to Superhydrophobic ratio (A*) %
D100	100	900	0.8
D200	200	800	3.2
D300	300	700	7.6
D400	400	600	14.4
D500	500	500	24.4
D600	600	400	39.4
D700	700	300	62.6
D800	800	200	101.1
D900	900	100	174.9
SPho	Totally Superhydrophobic		
Pho	Totally Hydrophobic		
Phi	Totally Hydrophilic		

The protocol described above was followed to fabricate nine biphilic surfaces, each surface having a different islands diameter. **Table 3**. tabulates detailed geometrical properties of these surfaces. Superhydrophobic SPho, plain hydrophobic Pho, and hydrophilic Phi surfaces are used for comparison purposes. The number in front of D stands for the island diameter in μm such that

D100 represents the biphilic surface with island diameter of 100 μm. Since a pitch size of (P=1 mm) between hydrophobic islands was kept constant for all the biphilic surfaces, the edge-to-edge distance between islands S was dependent on the islands diameter D. To determine the ratio of hydrophobic to superhydrophobic surface area, a new parameter (A*=$A_{hydrophobic}$/$A_{superhydrophobic}$) was defined.
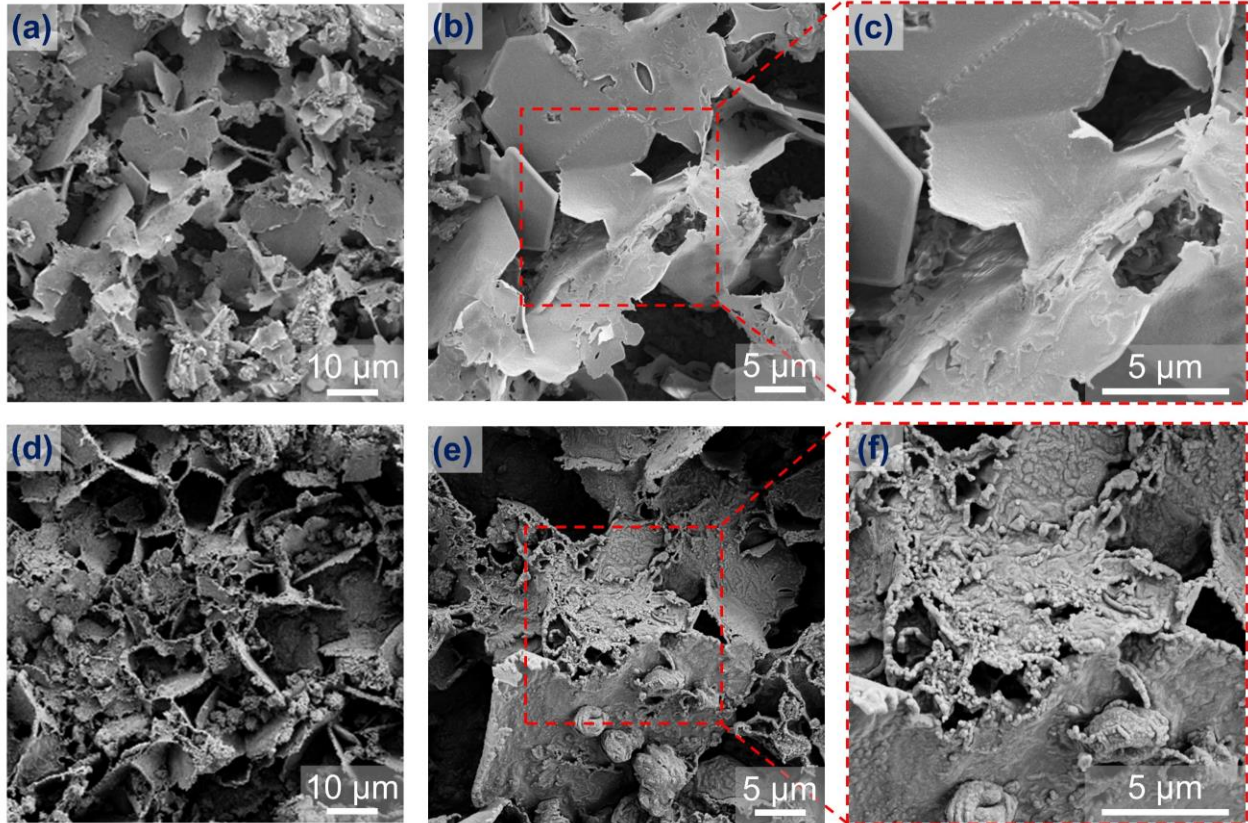
Figure 20. SEM images: (a, b, c) before Chromium deposition, and (d, e, f) after Chromium deposition. (a) SEM images shows flake shape nanostructures formed on the surface after wet etching. (b, c) Magnified SEM image before Chromium deposition. (d) SEM image of Chromium nano particles after e-beam PVD deposition. (d, e) Magnified SEM image, which shows a thin layer of Chromium nanoparticles deposited on the surface after PVD deposition.

4.2.2 Surface Characterization

Figure 20a, b, and c show SEM images of the nanostructured surface before Chromium deposition in different magnifications. It is well established in the literature that wet chemical etching of copper leads to the formation of flake shaped nanostructures on the surface[49,82,95]. These nanostructures play an important role in surface wettability and droplet morphology during

condensation. **Figure 20**d, e, and f show SEM images of the nanostructured surface after Chromium deposition via the Electron Beam PVD Deposition Technique. Magnified SEM images show that thin layer (150 nm thick) of Chromium nanoparticles can be deposited on the surface upon e-beam PVD deposition.
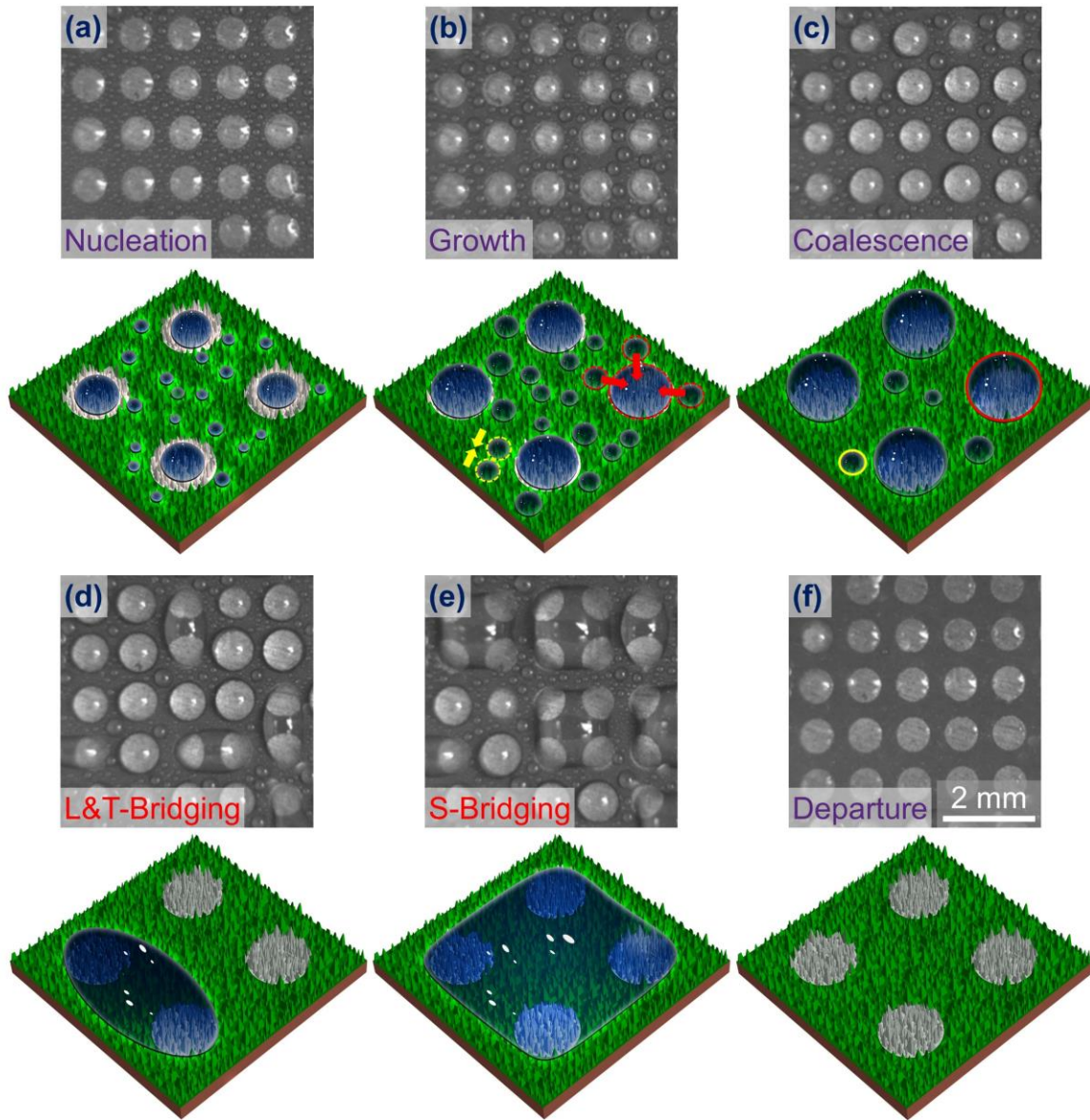
Figure 21. Droplet Dynamics on a biphilic surface D700 (with islands diameter of $D = 700$) during a full flow condensation cycle at steam mass flux of 10 kg/m^{2}s. (a) Droplet Nucleation on both hydrophobic islands and superhydrophobic areas. (b) Droplet growth. (c) Droplet coalescence. (d) Formation of longitudinal and transverse bridges. (e) Formation of square bridges. (d) Droplet departure. The schematic below each real time image gives more clarification regarding the behavior of droplets at the corresponding stage. The yellow circles on the schematic

41

of (b, c) show two droplets on the superhydrophobic area right before and after coalescence, respectively. The red circles on the schematic of (b, c) show the droplets right before and after coalescence with the droplet on the hydrophobic spot, respectively.

Contact angle measurement of 5 μL droplets were done via Attension® Theta Lite optical tensiometer. The contact angle results were obtained by averaging six sessile contact angle measurements from different portions of the sample which lead to average droplet contact angle of 172º and 131º for superhydrophobic and hydrophobic, respectively.

4.3   Results and Discussion

Flow condensation experiments were conducted at five different steam mass fluxes of 10, 20, 30, 40 and 50 kg/m²s at the cooling water mass flowrate of 9.11 g/s in a minichannel. The experimental flow loop used in our previous study was utilized to perform the condensation heat transfer tests[95]. Steam enters the test section at saturation the pressures and temperatures of 102-130 kPa and 100.2-107.2 °C, respectively, depending on the inlet steam mass flux. A superheater was utilized to ensure that the steam entering the pre-condenser was superheated about 1˚C above the saturation temperature. Besides the heat transfer analysis, visualization studies were simultaneously performed using the high-speed camera system. Real-time images of dropwise condensation were captured with the sampling rate of 2000 frames per second with the resolution of 256×256 pixels.

4.3.1   Visualization Study

To investigate droplet dynamics on a biphilic surface during a full flow condensation cycle, a visualization study was performed at steam mass flux of 10 kg/m²s. A full dropwise condensation cycle consists of four stages of droplet nucleation, droplet growth, droplet coalescence, and droplet departure. **Figure 21** shows the real time images obtained by the high-speed camera of a full condensation cycle on a biphilic surface D700 (hydrophobic islands with diameter of *D*=700μm) with the ratio of hydrophobic to superhydrophobic surface area of A*=62.6%. The schematic below each real time image gives more clarification regarding the behavior of droplets at the corresponding stage. **Figure 21**a shows droplet nucleation on both hydrophobic islands and superhydrophobic areas. As seen, due to the higher wettability of the hydrophobic islands compared to the superhydrophobic areas, the embryos preferentially nucleate earlier and faster on

the hydrophobic patterns[92]. **Figure 21**b and c illustrate growth and coalescence of the nucleated droplets. The yellow circles on the schematic of (b, c) show two droplets on the superhydrophobic area right before and after coalescence, respectively. The red circles on the schematic of (b, c) show the droplets right before and after coalescence with the droplet on the hydrophobic spot, respectively. As the droplets grow on the superhydrophobic regions, some of them are pumped into the hydrophobic islands as a result of capillary pressure difference[68,96,97] (red circles on **Figure 21**b and c).

The size and volume of the droplets on the hydrophobic islands continue increasing as the droplets in their near surrounding are pumped into them. As the size and volume of the droplets on the hydrophobic islands increase, the two droplets on the hydrophobic islands merge together and create longitudinal and transverse bridges[98] if the edge-to-edge distance between two hydrophobic islands is small enough (**Figure 21**d).

When the vapor shear is not enough to detach the merged droplets from the surface, square bridging might also occur on the patterned surface, where four droplets on the patterned areas merge (**Figure 21**e). The liquid formed on the surface acts as an insulation layer and imposes thermal resistance to the system. Consequently, bridges formed on the patterned areas deteriorate thermal performance. Therefore, in designing biphilic surfaces for condensation heat transfer, it is very crucial to design surfaces avoiding occurrence of the bridging phenomena. More detailed discussion regarding the optimum diameter of the biphilic islands for condensation heat transfer for avoiding bridging phenomena is made in section 4.3.2.

After droplets grow and reach their critical size, they depart from the surface as shown in **Figure 21**f. Neglecting the gravity, the balance between two forces, the vapor shear force (in the direction of the flow) and droplet adhesion force (opposite to the direction of the flow), is the main mechanism responsible for droplet departure in flow condensation. When the vapor shear force acting on the interface of a condensed droplet overcomes the droplet-surface adhesion force, the droplets start to sweep away from the surface[93,94]. A very detailed discussion about the droplet departure mechanism on the hydrophobic/superhydrophobic surfaces could be found in our previous study[95].

To gain insight into the effect of steam mass flux on the behavior of droplets during flow condensation on a biphilic surface, a more detailed study is performed. **Figure 22** shows droplet distribution just before departure at various steam mass fluxes on two different surfaces. A biphilic

surfaces D700 (islands diameter of 700 μm) and a plain hydrophobic surface are shown in **Figure 22**a and b, respectively.
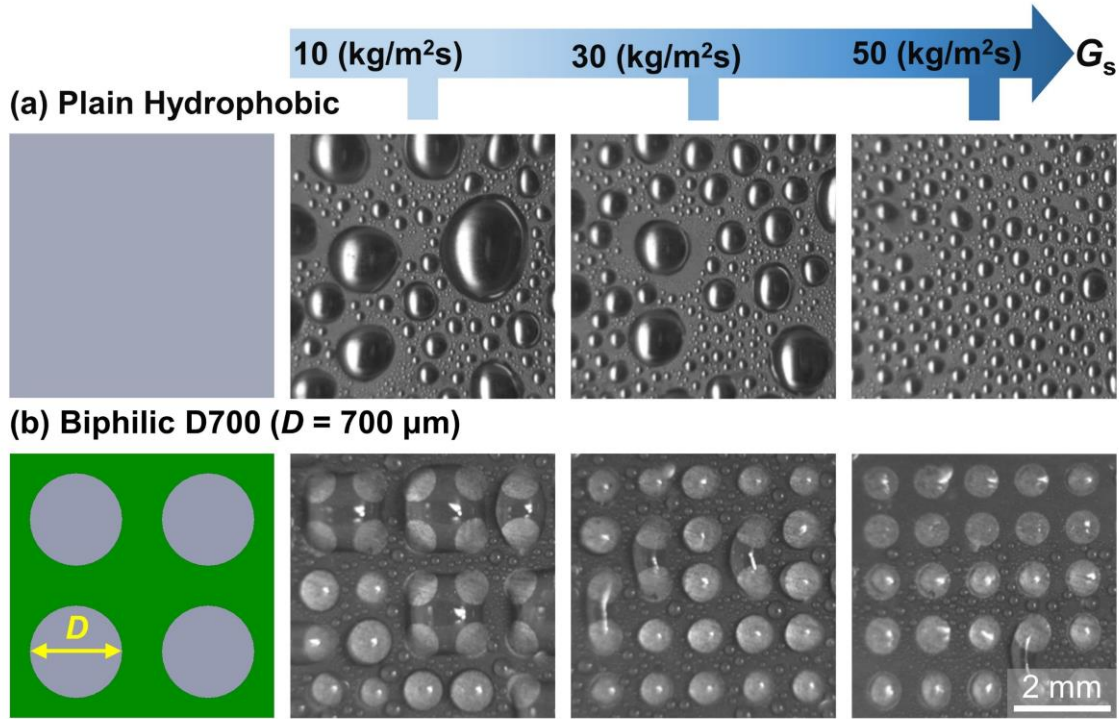
Figure 22. Behavior of droplets on (a) Plain hydrophobic and (b) Biphilic D700 under different steam mass fluxes.

(**Figure 22**a) shows discrete droplets ranging from micrometers to millimeters, which cover the entire surface. Conventional dropwise condensation, which is distinguished by discrete droplet formation and removal instead of formation of liquid film, is observed on non-wetting (hydrophobic/superhydrophobic) surfaces. Due to the enhanced droplet mobility, dropwise condensation substantially enhances the condensation heat transfer performance. As seen, the increase in the vapor velocity reduces the size of the departing droplets on the hydrophobic surface. The increase in the vapor velocity increases the shear force acting on the droplet. A droplet departs from the surface, when the shear force acting on the interface of the droplet reaches to a critical value. This occurs when either the size of the droplet or the steam mass flux reaches the critical value. In our previous study, we demonstrate that although the force analysis on droplets in confined channels could be a complex process, the simplified analysis could be done to clarify that the droplet departure diameter decreases with the steam velocity. As seen in Figure 22a, when the

mass flux increases from 10 to 30 kg/m2s, droplet departure diameters considerably decrease in size. This decrease even is more significant when the mass flux is increased from 30 to 50 kg/m^{2}s. In our previous study, we showed that on a superhydrophobic surface, the size of the droplets gets even smaller and hence the droplet departure frequency increases when compared to plain hydrophobic surface. However, for the biphilic surface D700, Figure 22b, shows that at mass flux of 10 kg/m^{2}s, very large liquid bridges could be formed on the surface, and the condensation performance significantly deteriorates. The droplets tend to nucleate earlier and grow on the hydrophobic islands because of the higher wettability. Some of the droplets growing on the superhydrophobic regions migrate to the hydrophobic islands due to the capillary pressure difference and get even bigger in size and volume. This is due to the patterns with very large islands diameter and small edge to edge distance (S = 300µm) of this surface so that two droplets on the hydrophobic island merge and form bridges. However, when the steam mass flux increases to 30 kg/m^{2}s, because of the increased mobility of the droplets due to the increased vapor shear force, the square bridges disappear from the surface. Although the droplets are more mobile at steam mass flux of 30 kg/m^{2}s compared to mass flux of 10 kg/m2s, some transverse and longitudinal bridges might occur on the surface. When the steam mass flux is further increased to 50 kg/m^{2}s, the number of bridges is significantly reduced, and the thermal performance is considerably enhanced as discussed in section 4.3.2. Due to the increased vapor drag, the droplets on the surface are detached from the surface before they can reach the critical size to form the bridges.
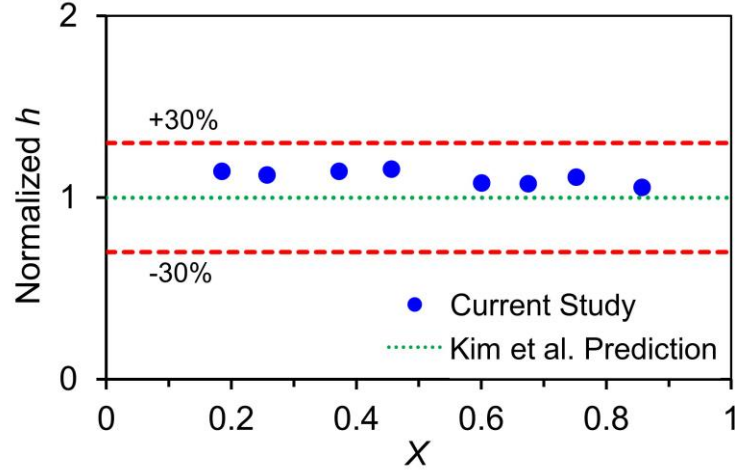
Figure 23. Comparison of the experimental heat transfer coefficients data with the predictions of the Kim and Mudawar's correlation for the filmwise condensation on a hydrophilic copper surface. X is the average vapor quality.

4.3.2   Heat Transfer Analysis

Before quantifying the heat transfer performance of the biphilic surfaces, the experimental data for filmwise condensation on hydrophilic copper surface was compared with the predictions of the Kim and Mudawar's correlation[77,86]. The accuracy of the obtained data for filmwise condensation was evaluated by the mean absolute error (MAE) defined as:

$$MAE = \frac{1}{M} \sum_{i=1}^{M} \frac{\left| h_{\text{pred}} - h_{\text{exp}} \right|}{h_{\text{exp}}} \times 100\% \tag{1}$$

where h_{pred}, and h_{exp} are the predicted and the experimental heat transfer coefficients which are obtained as:

$$h_{\text{pred}} = \frac{k_{\text{f}}}{D_{\text{h}}} 0.048 Re_{\text{f}}^{0.69} Pr_{\text{f}}^{0.34} \frac{\phi_{\text{g}}}{X_{\text{tt}}} \tag{2}$$

$$h = \frac{1}{3} \sum_{j=1}^{3} h_j = \frac{1}{3} \sum_{j=1}^{3} \frac{q_j}{T_{\text{sat}} - T_{\text{s},j}} \tag{3}$$

The heat flux (q) in equation 3 is calculated as:

$$q = \frac{1}{3}\sum_{j=1}^{3} q_j = \frac{1}{3}\sum_{j=1}^{3} -k \frac{\sum_{i=1}^{4}\left(y_{i,j} - \overline{y_j}\right)\left(T_{i,j} - \overline{T_j}\right)}{\sum_{i=1}^{4}\left(y_{i,j} - \overline{y_j}\right)^2} \qquad (4)$$

Figure 23. shows the normalized condensation heat transfer coefficient (Normalized h) as a function of mean steam quality X. Normalized h values for the Kim and Mudawar's correlation are obtained by $h_{prediction}/h_{prediction}$, which resulted in unity. These values for the current experimental study are obtained with the ratio of $h_{experimental}/h_{prediction}$. As can be seen, the experimental results and predictions of the Kim and Mudawar's correlation show agood agreement with a MAE of 10.5%. The uncertainties associated with the mean heat transfer coefficient and the mean vapor quality are ±6.6%, and ±7.3%, respectively, which were obtained using the uncertainty propagation method[81].
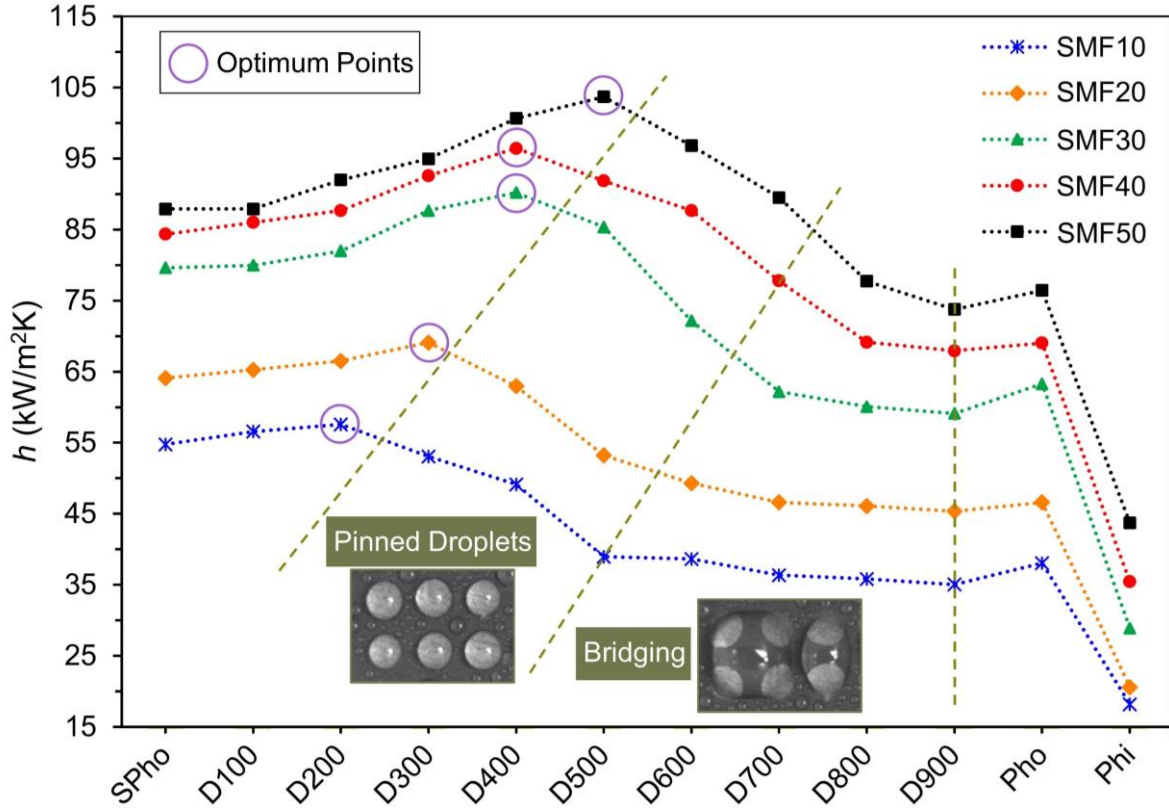
Figure 24. Condensation heat transfer performance at different steam mass fluxes *SMF*. Heat transfer coefficient h is on the vertical axis and nine biphilic surfaces with different islands diameter D are on the horizontal axis. The number in front of D represents the island diameter in μm. Superhydrophobic SPho, plain hydrophobic Pho, and hydrophilic Phi surfaces are included for comparison purposes.

Figure 24 shows the condensation heat transfer coefficient h at different steam mass fluxes *SMF* for nine biphilic surfaces with different islands diameters D. The number in front of *SMF* shows the value of the steam mass flux in kg/m^{2}s. The number in front of D represents the island diameter in μm such that the D700 represents the biphilic surface with 700 μm hydrophobic islands diameter. The superhydrophobic surface without any islands SPho as well as plain hydrophobic Pho, and hydrophilic Phi surfaces are included for comparison purposes.

As seen, the condensation heat transfer coefficient increases with the steam mass flux for all the tested samples. However, the rate of enhancement is dependent on the surface properties. The vapor shear force, as the driving force for droplet removal in dropwise flow condensation, increases with steam mass flux. As a result, droplets are removed from the surface because of the vapor shear force acting on the interface of the condensed droplet. The removal of the grown droplets from the surface allows nucleation of new droplets on the surface, which enhances the condensation heat transfer performance.

For all the steam mass fluxes, the heat transfer coefficient increases with island diameter until it reaches the maximum values of 58, 69, 90, 96, and 104 kW/m^{2}K for steam mass flux of 10, 20, 30, 40, and 50 kg/m^{2}s. These maximum points correspond to biphilic surfaces with the island diameters of 200, 300, 400, 400, and 500 μm, with ratios of hydrophobic to superhydrophobic surface area (A*=A$_{hydrophobic}$/A$_{superhydrophobic}$) of 3.2, 7.6, 14.4, 14.4, 24.4%. respectively. After the increasing trend, the heat transfer coefficient decreases with the island diameter. As the islands diameter further increase, heat transfer coefficient decreases substantially. Based on the trend of heat transfer coefficient with different surfaces, the heat transfer coefficient curve can be divided into three sections. Each of the three sections can be associated with a different droplet behavior on the condensing surfaces.

The first section, where the heat transfer performance increases with the island diameter, corresponds to the enhanced droplet nucleation and rapid sweeping region. The enhancement observed in this region is not only because of the spatial control of droplet nucleation but it is also influenced by the increase in sweeping period. The energy barrier ΔG for the initial nucleation of droplets can be calculated as $\Delta G = \pi r_{min}^2 \sigma \left(2 - 3\cos\theta + \cos^3\theta\right)/3$ according to Volmer's nucleation theory[92], where r_{min} is minimum nucleation radius, σ is surface tension of water, and θ is contact angle. Based on this expression, the energy barrier for droplet nucleation on a hydrophobic surface (lower contact angle θ) is lower compared to a superhydrophobic surface

(higher contact angle θ). As a result, droplets prefer to nucleate on the hydrophobic islands with a smaller energy barrier compared to the superhydrophobic areas with a higher energy barrier.

The second section, where heat transfer coefficient starts to decrease, corresponds to highly pinned droplets. As the island diameter increases, the formation of larger pinned droplets decreases the sweeping period. Consequently, the heat transfer coefficient decreases in this region.

The third section corresponds to the formation of bridging droplets on the condensing surfaces. Bridging phenomena generally occur on the surfaces with larger islands diameter, where the edge-to-edge distance S of the hydrophobic islands decreases, as discussed in more detail in the visualization study **Figure 21** and **Figure 22**. The liquid bridging formed on the surface acts as a thermal resistance leading to a reduction in condensation heat transfer performance. Therefore, a further enhancement of condensation heat transfer with increasing islands diameter is challenging due to the bridging phenomena. Preferential droplet nucleation occurs on hydrophobic islands with larger diameters, with low edge to edge distance, which results in coalescence of highly pinned droplets on the hydrophobic islands and promotion of bridging phenomena.

Although the thermal performance of biphilic surfaces with 800, and 900 μm diameter (*D*800, and *D*900) are generally lower than the plain hydrophobic surface, for all other biphilic surfaces condensation heat transfer is enhanced compared to the plain hydrophobic surface. Specifically, considering the optimum point for each steam mass flux having the best heat transfer performance (indicated by purple circles), the condensation heat transfer coefficient is increased by 51, 48, 42, 40, and 36% compared to the plain hydrophobic surface for steam mass fluxes of 10, 20, 30, 40, and 50 kg/m^{2}s corresponding to biphilic surfaces with diameter of 200, 300, 400, 400, and 500 μm, respectively. These maximum points (indicated by purple circles on **Figure 24**) imply that there is an optimum island diameter for each steam mass flux, where heat transfer performance is maximum. For the steam mass fluxes of 10, 20, 30, 40, and 50 kg/m^{2}s, the optimum island diameter is obtained as 200, 300, 400, 400, and 500 μm, with the ratio of hydrophobic to superhydrophobic surface area ($A^*=A_{hydrophobic}/A_{superhydrophobic}$) of 3.2, 7.6, 14.4, 14.4, 24.4%, respectively. The highest heat transfer coefficient observed in this experiment ($h = 104$ kW/m^{2}K) is achieved at the mass flux of 50 kg/m^{2}s on the biphilic surface with the island diameter of 500 μm.
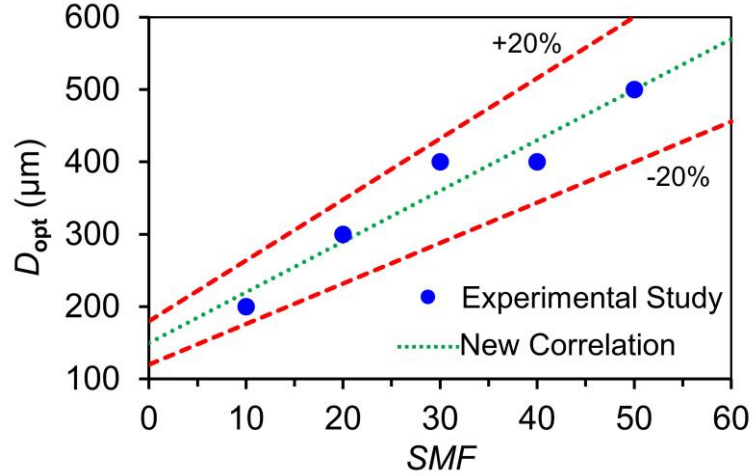
Figure 25. Comparison of the experimental data with the predictions of the developed new correlation. Optimum islands diameter (D_{opt}) as a function of steam mass flux (*SMF*). The new correlation predicts the data with a MAE of 6.2%.

4.3.3   Development of a New Correlation

Figure 25. shows the optimum islands diameter (D_{opt}) of the hydrophobic spots on a superhydrophobic surface SPho as a function of thesteam mass flux (*SMF*). The Least Squares Method was employed in fitting the experimental data to obtain a correlation for prediction the optimum island diameter of the biphilic surfaces during flow condensation as a function of steam mass flux in the range of 10-50 kg/m^{2}s. The correlation predicted the data with a MAE of 6.2% and is expressed as:

$$D_{opt} = 7(SMF) + 150 \qquad (5)$$

While this correlation has certain constraints such as constant pitch distance between hydrophobic islands, constant channel hydraulic diameter, and a confined range of steam mass fluxes, efforts will be made in further studies to develop a more universal correlation.

5 CONCLUSION

In this thesis, two different types of surfaces, namely superhydrophobic and biphilic surfaces were investigated for flow condensation heat transfer enhancement.

In the light of findings of this thesis, the following conclusions are drawn:

- Our visualization study on nanostructured superhydrophobic surfaces displayed that an increase in the steam mass flux led to a reduction in the droplet departure diameter and cycle time, resulting in a shift in the droplet diameter distribution.

- An increase in the steam quality enhanced heat transfer because of lower liquid content of the flow, which resulted in a reduction in the thermal resistance associated with saturated liquid.

- As the driving force of condensation, an increase in the coolant water mass flow rate promoted the formation of large pinned droplets, leading to an increase in the cycle time and refreshing period and causing a reduction in the heat transfer coefficient.

- A simplified analytical approach was provided to elaborate on the forces acting on a condensed droplet and their effect on the droplet departure. The analytical approach agreed with the experimental data in explaining the relationship between the vapor velocity and the droplet departure radius.

- The combined effect of the increase in mass flux and excellent water repellency characteristics of nanostructured superhydrophobic surfaces led to an enhancement of 33% in flow condensation heat transfer in dropwise condensation on a superhydrophobic surface compared to a conventional hydrophobic surface.

In addition, the study of steam flow condensation through a minichannel on biphilic surfaces has the following major conclusions:

- Based on the trend of heat transfer coefficient with different biphilic surfaces, the heat transfer coefficient curve can be divided into three regions of the enhanced droplet nucleation and rapid sweeping region, highly pinned droplets region, and bridging droplets region. The enhancement observed in enhanced droplet nucleation and rapid

sweeping region is due to both spatial control of droplet nucleation and increase in the sweeping period.

- There exist optimum island diameters D of the hydrophobic islands on a superhydrophobic background as a function of steam mass flux, where heat transfer performance is maximum.

- For steam mass fluxes of 10, 20, 30, 40, and 50 kg/m²s, the optimum island diameters are obtained as 200, 300, 400, 400, and 500 μm, with ratio of hydrophobic to superhydrophobic surface area ($A^*=A_{hydrophobic}/A_{superhydrophobic}$) of 3.2, 7.6, 14.4, 14.4, 24.4%, respectively.

- Compared to the plain hydrophobic surface, the surfaces with the optimum islands diameter, enhance condensation heat transfer by 51, 48, 42, 40, and 36% for steam mass fluxes of 10, 20, 30, 40, and 50 kg/m²s, respectively.

- Very high heat transfer coefficient of up to $h = 104$ kW/m²K is achieved on the biphilic surface with the island diameter of 500 μm at the steam mass flux of 50 kg/m²s.

- A correlation for the prediction the optimum island diameter of the biphilic surfaces as a function of steam mass flux is recommended. The correlation predicted the experimental data with a MAE of 6.2%

REFERENCES

(1) Bergman, T.; Incropera, F.; DeWitt, D.; Lavine, A. *Fundamentals of Heat and Mass Transfer*; Wiley Custom Learning Solutions: Hoboken, NJ, 2011.

(2) Zhao, B.; Wang, L. Y.; Chung, T. S. Enhanced Membrane Systems to Harvest Water and Provide Comfortable Air via Dehumidification & Moisture Condensation. *Sep. Purif. Technol.* **2019**. https://doi.org/10.1016/j.seppur.2019.03.034.

(3) Lukic, N.; Diezel, L. L.; Fröba, A. P.; Leipertz, A. Economical Aspects of the Improvement of a Mechanical Vapour Compression Desalination Plant by Dropwise Condensation. *Desalination* **2010**. https://doi.org/10.1016/j.desal.2010.07.023.

(4) Mudawar, I. Assessment of High-Heat-Flux Thermal Management Schemes. *IEEE Trans. Components Packag. Technol.* **2001**, *24* (2), 122–141. https://doi.org/10.1109/6144.926375.

(5)   Bao, J.; Lin, Y.; Zhang, R.; Zhang, N.; He, G. Strengthening Power Generation Efficiency Utilizing Liquefied Natural Gas Cold Energy by a Novel Two-Stage Condensation Rankine Cycle (TCRC) System. *Energy Convers. Manag.* **2017**. https://doi.org/10.1016/j.enconman.2017.04.018.

(6)   Wang, S.; Yu, X.; Liang, C.; Zhang, Y. Enhanced Condensation Heat Transfer in Air-Conditioner Heat Exchanger Using Superhydrophobic Foils. *Appl. Therm. Eng.* **2018**, *137*, 758–766. https://doi.org/10.1016/j.applthermaleng.2018.04.020.

(7)   Dounis, A. I.; Caraiscos, C. Advanced Control Systems Engineering for Energy and Comfort Management in a Building Environment-A Review. *Renewable and Sustainable Energy Reviews*. 2009. https://doi.org/10.1016/j.rser.2008.09.015.

(8)   Rao, Z.; Wang, S.; Wu, M.; Lin, Z.; Li, F. Experimental Investigation on Thermal Management of Electric Vehicle Battery with Heat Pipe. *Energy Convers. Manag.* **2013**. https://doi.org/10.1016/j.enconman.2012.08.014.

(9)   Rose, J. W. Condensation Heat Transfer Fundamentals. *Chem. Eng. Res. Des.* **1998**, *76* (2), 143–152. https://doi.org/10.1205/026387698524712.

(10)   Rose, J. W. Dropwise Condensation Theory and Experiment: A Review. *Proc. Inst. Mech. Eng. Part A J. Power Energy* **2002**, *216* (2), 115–128. https://doi.org/10.1243/09576500260049034.

(11)   Schmidt, E.; Schurig, W.; Sellschopp, W. Versuche Über Die Kondensation von Wasserdampf in Film- Und Tropfenform. *Tech. Mech. und Thermodyn.* **1930**, *1* (2), 53–63. https://doi.org/10.1007/BF02641051.

(12)   O'neill, G. A.; Westwater, J. W. Dropwise Condensation of Steam on Electroplated Silver Surfaces. *Int. J. Heat Mass Transf.* **1984**, *27* (9), 1539–1549. https://doi.org/10.1016/0017-9310(84)90266-7.

(13)   Lee, Y. L.; Fang, T. H.; Yang, Y. M.; Maa, J. R. The Enhancement of Dropwise Condensation by Wettability Modification of Solid Surface. *Int. Commun. Heat Mass Transf.* **1998**. https://doi.org/10.1016/S0735-1933(98)00100-6.

(14)   Kandlikar, S. G. *Handbook of Phase Change: Boiling and Condensation*; Taylor and Francis, an imprint of Routledge: Boca Raton, FL, 2019.

(15)   Chen, C.-H.; Cai, Q.; Tsai, C.; Chen, C.-L.; Xiong, G.; Yu, Y.; Ren, Z. Dropwise Condensation on Superhydrophobic Surfaces with Two-Tier Roughness. *Appl. Phys. Lett.*

2007, *173108* (December 2006). https://doi.org/10.1063/1.2731434.

(16)   Dietz, C.; Rykaczewski, K.; Fedorov, A. G.; Joshi, Y. Visualization of Droplet Departure on a Superhydrophobic Surface and Implications to Heat Transfer Enhancement during Dropwise Condensation. *Appl. Phys. Lett.* **2010**, *97* (3), 033104. https://doi.org/10.1063/1.3460275.

(17)   Das, A. K.; Kilty, H. P.; Marto, P. J.; Andeen, G. B.; Kumar, A. The Use of an Organic Self-Assembled Monolayer Coating to Promote Dropwise Condensation of Steam on Horizontal Tubes. *J. Heat Transfer* **2000**, *122* (2), 278–286. https://doi.org/10.1115/1.521465.

(18)   Zhong, L.; Xuehu, M.; Sifang, W.; Mingzhe, W.; Xiaonan, L. Effects of Surface Free Energy and Nanostructures on Dropwise Condensation. *Chem. Eng. J.* **2010**, *156* (3), 546–552. https://doi.org/10.1016/j.cej.2009.04.007.

(19)   Zhang, W.; Ding, W.; Fernandino, M.; Dorao, C. A. Water-Repellent Surfaces Consisting of Nanowires on Micropyramidal Structures. *ACS Appl. Nano Mater.* **2019**, *2* (12), 7696–7704. https://doi.org/10.1021/acsanm.9b01767.

(20)   Fang, C.; Steinbrenner, J. E.; Wang, F. M.; Goodson, K. E. Impact of Wall Hydrophobicity on Condensation Flow and Heat Transfer in Silicon Microchannels. *J. Micromechanics Microengineering* **2010**, *20* (4). https://doi.org/10.1088/0960-1317/20/4/045018.

(21)   Derby, M. M.; Chatterjee, A.; Peles, Y.; Jensen, M. K. Flow Condensation Heat Transfer Enhancement in a Mini-Channel with Hydrophobic and Hydrophilic Patterns. *Int. J. Heat Mass Transf.* **2014**, *68*, 151–160. https://doi.org/10.1016/j.ijheatmasstransfer.2013.09.024.

(22)   Shi, J.; Zheng, G.; Chen, Z.; Dang, C. Experimental Study of Flow Condensation Heat Transfer in Tubes Partially Filled with Hydrophobic Annular Metal Foam. *Int. J. Heat Mass Transf.* **2019**, *136*, 1265–1272. https://doi.org/10.1016/j.ijheatmasstransfer.2019.03.039.

(23)   Chen, X.; Derby, M. M. Combined Visualization and Heat Transfer Measurements for Steam Flow Condensation in Hydrophilic and Hydrophobic. *J. Heat Transfer* **2016**, *138* (September), 1–11. https://doi.org/10.1115/1.4033496.

(24)   Chen, X.; Morrow, J. A.; Derby, M. M. Mini-Channel Flow Condensation Enhancement through Hydrophobicity in the Presence of Noncondensable Gas. *Int. J. Heat Mass Transf.* **2017**, *115*, 11–18. https://doi.org/10.1016/j.ijheatmasstransfer.2017.07.029.

(25)   Yuan, J.; Wang, Y.; Xu, J.; Ji, X.; Xie, J. Convective Dropwise Condensation Heat Transfer

in Mini-Channels with Biphilic Surface. *Int. J. Heat Mass Transf.* **2019**, *134*, 69–84. https://doi.org/10.1016/j.ijheatmasstransfer.2019.01.015.

(26)   Wang, H.; Nguyen, Q.; Kwon, J. W.; Ma, H. Condensation and Wetting Behavior on Hybrid Superhydrophobic and Superhydrophilic Copper Surfaces. *J. Heat Transfer* **2020**, *142* (4). https://doi.org/10.1115/1.4046209.

(27)   Song, Z.; Lu, M.; Chen, X. Investigation of Dropwise Condensation Heat Transfer on Laser-Ablated Superhydrophobic/Hydrophilic Hybrid Copper Surfaces. *ACS Omega* **2020**, *5* (37), 23588–23595. https://doi.org/10.1021/acsomega.0c01995.

(28)   Li, Q.; Luo, K. H.; Kang, Q. J.; He, Y. L.; Chen, Q.; Liu, Q. Lattice Boltzmann Methods for Multiphase Flow and Phase-Change Heat Transfer. *Progress in Energy and Combustion Science*.   Elsevier   Ltd   February   1,   2016,   pp   62–105. https://doi.org/10.1016/j.pecs.2015.10.001.

(29)   Ma, X.; Cheng, P.; Quan, X. Simulations of Saturated Boiling Heat Transfer on Bio-Inspired Two-Phase Heat Sinks by a Phase-Change Lattice Boltzmann Method. *Int. J. Heat Mass Transf.* **2018**, *127*, 1013–1024. https://doi.org/10.1016/j.ijheatmasstransfer.2018.07.082.

(30)   Zhao, W.; Gao, Y.; Li, R.; Qiu, S.; Zhang, Y.; Xu, B. Hybrid Phase-Change Lattice Boltzmann Simulation of Vapor Condensation on Vertical Subcooled Walls. *J. Heat Transfer* **2020**, *142* (4). https://doi.org/10.1115/1.4046304.

(31)   Wang, X.; Xu, B.; Chen, Z.; Yang, Y.; Cao, Q. Lattice Boltzmann Modeling of Condensation Heat Transfer on Downward-Facing Surfaces with Different Wettabilities. *Langmuir* **2020**, *36* (31), 9204–9214. https://doi.org/10.1021/acs.langmuir.0c01469.

(32)   Li, M.; Qu, J.; Ocłoń, P.; Wei, J.; Tao, W. 3D Numerical Simulation of Condensation and Condensate Behaviors on Textured Structures Using Lattice Boltzmann Method. *Int. J. Heat   Mass   Transf.*   **2020**,   *160*,   120198. https://doi.org/10.1016/j.ijheatmasstransfer.2020.120198.

(33)   Zhang, C.; Shen, C.; Chen, Y. Experimental Study on Flow Condensation of Mixture in a Hydrophobic Microchannel. *Int. J. Heat Mass Transf.* **2017**, *104*, 1135–1144. https://doi.org/10.1016/j.ijheatmasstransfer.2016.09.029.

(34)   Garimella, S.; Milkie, J.; Macdonald, M. Condensation of Zeotropic Mixtures of Low-Pressure Hydrocarbons and Synthetic Refrigerants. *Int. J. Heat Mass Transf.* **2020**. https://doi.org/10.1016/j.ijheatmasstransfer.2020.120301.

(35) Dong, T.; Yang, Z. Measurement and Modeling of R141b Condensation Heat Transfer in Silicon Rectangular Microchannels. *J. Micromechanics Microengineering* **2008**, *085012*, 085012. https://doi.org/10.1088/0960-1317/18/8/085012.

(36) Ding, Y.; Jia, L.; Zhang, Y.; An, Z. Investigation on R141b Convective Condensation in Microchannel with Low Surface Energy Coating and Hierarchical Nanostructures Surface. *Appl. Therm. Eng.* **2019**, *155* (March), 480–488. https://doi.org/10.1016/j.applthermaleng.2019.04.023.

(37) Rahman, M. M.; Kariya, K.; Miyara, A. An Experimental Study and Development of New Correlation for Condensation Heat Transfer Coefficient of Refrigerant inside a Multiport Minichannel with and without Fins. *Int. J. Heat Mass Transf.* **2018**, *116*, 50–60. https://doi.org/10.1016/j.ijheatmasstransfer.2017.09.010.

(38) Gu, X.; Wen, J.; Wang, C.; Zhang, X.; Wang, S.; Tu, J. Condensation Flow Patterns and Model Assessment for R1234ze(E) in Horizontal Mini/Macro-Channels. *Int. J. Therm. Sci.* **2018**, *134*, 140–159. https://doi.org/10.1016/j.ijthermalsci.2018.08.006.

(39) Miljkovic, N.; Enright, R.; Wang, E. N. Effect of Droplet Morphology on Growth Dynamics and Heat Transfer during Condensation on Superhydrophobic Nanostructured Surfaces. *ACS Nano* **2012**, *6* (2), 1776–1785. https://doi.org/10.1021/nn205052a.

(40) Miljkovic, N.; Wang, E. N. Condensation Heat Transfer on Superhydrophobic Surfaces. *MRS Bull.* **2013**, *38* (5), 397–406. https://doi.org/10.1557/mrs.2013.103.

(41) Enright, R.; Miljkovic, N.; Alvarado, J. L.; Kim, K.; Rose, J. W. Dropwise Condensation on Micro- and Nanostructured Surfaces. *Nanoscale Microscale Thermophys. Eng.* **2014**, *18* (3), 223–250. https://doi.org/10.1080/15567265.2013.862889.

(42) Lv, C.; Hao, P.; Yao, Z.; Niu, F. Departure of Condensation Droplets on Superhydrophobic Surfaces. *Langmuir* **2015**. https://doi.org/10.1021/la504638y.

(43) Lv, C.; Hao, P.; Zhang, X.; He, F. Dewetting Transitions of Dropwise Condensation on Nanotexture- Enhanced Superhydrophobic Surfaces. *ACS Nano* **2015**, No. 12, 12311–12319. https://doi.org/10.1021/acsnano.5b05607.

(44) Chu, F.; Wu, X. Fabrication and Condensation Characteristics of Metallic Superhydrophobic Surface with Hierarchical Micro-Nano Structures. *Appl. Surf. Sci.* **2016**, *371*, 322–328. https://doi.org/10.1016/j.apsusc.2016.02.208.

(45) Yin, L.; Wang, Y.; Ding, J.; Wang, Q.; Chen, Q. Water Condensation on Superhydrophobic

Aluminum Surfaces with Different Low-Surface-Energy Coatings. *Appl. Surf. Sci.* **2012**, *258* (8), 4063–4068. https://doi.org/10.1016/j.apsusc.2011.12.100.

(46)   Oberli, L.; Caruso, D.; Hall, C.; Fabretto, M.; Murphy, P. J.; Evans, D. Condensation and Freezing of Droplets on Superhydrophobic Surfaces. *Advances in Colloid and Interface Science*. Elsevier 2014, pp 47–57. https://doi.org/10.1016/j.cis.2013.10.018.

(47)   Rykaczewski, K. Microdroplet Growth Mechanism during Water Condensation on Superhydrophobic Surfaces. *Langmuir* **2012**, *28* (20), 51. https://doi.org/10.1021/la301618h.

(48)   Varanasi, K. K.; Hsu, M.; Bhate, N.; Yang, W.; Deng, T. Spatial Control in the Heterogeneous Nucleation of Water. *Appl. Phys. Lett.* **2009**, *95* (9), 094101. https://doi.org/10.1063/1.3200951.

(49)   Miljkovic, N.; Enright, R.; Nam, Y.; Lopez, K.; Dou, N.; Sack, J.; Wang, E. N. Jumping-Droplet-Enhanced Condensation on Scalable Superhydrophobic Nanostructured Surfaces. *Nano Lett.* **2013**. https://doi.org/10.1021/nl303835d.

(50)   Boreyko, J. B.; Chen, C.-H. Self-Propelled Dropwise Condensate on Superhydrophobic Surfaces. *Phys. Rev. Lett.* **2009**, *103* (18), 184501. https://doi.org/10.1103/PhysRevLett.103.184501.

(51)   Chen, X.; Li, Q.; Hou, K.; Li, X.; Wang, Z. Microflower-Decorated Superhydrophobic Copper Surface for Dry Condensation. *Langmuir* **2019**, *35*, 22. https://doi.org/10.1021/acs.langmuir.9b02623.

(52)   Lu, M. C.; Lin, C. C.; Lo, C. W.; Huang, C. W.; Wang, C. C. Superhydrophobic Si Nanowires for Enhanced Condensation Heat Transfer. *Int. J. Heat Mass Transf.* **2017**, *111*, 614–623. https://doi.org/10.1016/j.ijheatmasstransfer.2017.04.021.

(53)   Parin, R.; Martucci, A.; Sturaro, M.; Bortolin, S.; Bersani, M.; Carraro, F.; Del Col, D. Nano-Structured Aluminum Surfaces for Dropwise Condensation. *Surf. Coatings Technol.* **2018**, *348* (May), 1–12. https://doi.org/10.1016/j.surfcoat.2018.05.018.

(54)   Ji, D. Y.; Lee, J. W.; Hwang, W.; Lee, K. Y. Experimental Study of Condensation Heat Transfer on a Horizontal Aluminum Tube with Superhydrophobic Characteristic. *Int. J. Heat Mass Transf.* **2019**, *134*, 286–295. https://doi.org/10.1016/j.ijheatmasstransfer.2019.01.040.

(55)   Wen, R.; Xu, S.; Zhao, D.; Lee, Y.-C.; Ma, X.; Yang, R. Hierarchical Superhydrophobic

Surfaces with Micropatterned Nanowire Arrays for High-Efficiency Jumping Droplet Condensation. *ACS Appl. Mater. Interfaces* **2017**. https://doi.org/10.1021/acsami.7b14960.

(56) Cai, S. Q.; Bhunia, A. Superhydrophobic Condensation Enhanced by Conical Hierarchical Structures. *J. Phys. Chem. C* **2017**. https://doi.org/10.1021/acs.jpcc.7b02554.

(57) Mulroe, M. D.; Srijanto, B. R.; Ahmadi, S. F.; Patrick Collier, C.; Boreyko, J. B. Tuning Superhydrophobic Nanostructures To Enhance Jumping-Droplet Condensation Article. *ACS Nano* **2017**, *11*, 5. https://doi.org/10.1021/acsnano.7b04481.

(58) Peng, Q.; Jia, L.; Guo, J.; Dang, C.; Ding, Y.; Yin, L.; Yan, Q. Forced Jumping and Coalescence-Induced Sweeping Enhanced the Dropwise Condensation on Hierarchically Microgrooved Superhydrophobic Surface. *Appl. Phys. Lett.* **2019**, *114* (13), 133106. https://doi.org/10.1063/1.5090360.

(59) Wang, R.; Zhu, J.; Meng, K.; Wang, H.; Deng, T.; Gao, X.; Jiang, L. Bio-Inspired Superhydrophobic Closely Packed Aligned Nanoneedle Architectures for Enhancing Condensation Heat Transfer. *Adv. Funct. Mater.* **2018**, *28* (49), 1800634. https://doi.org/10.1002/adfm.201800634.

(60) Wen, R.; Xu, S.; Ma, X.; Lee, Y. C.; Yang, R. Three-Dimensional Superhydrophobic Nanowire Networks for Enhancing Condensation Heat Transfer. *Joule* **2018**, *2* (2), 269–279. https://doi.org/10.1016/j.joule.2017.11.010.

(61) Wen, R.; Ma, X.; Lee, Y. C.; Yang, R. Liquid-Vapor Phase-Change Heat Transfer on Functionalized Nanowired Surfaces and Beyond. *Joule* **2018**, *2* (11), 2307–2347. https://doi.org/10.1016/j.joule.2018.08.014.

(62) Edalatpour, M.; Liu, L.; Jacobi, A. M.; Eid, K. F.; Sommers, A. D. Managing Water on Heat Transfer Surfaces: A Critical Review of Techniques to Modify Surface Wettability for Applications with Condensation or Evaporation. *Applied Energy*. Elsevier Ltd July 15, 2018, pp 967–992. https://doi.org/10.1016/j.apenergy.2018.03.178.

(63) Peng, B.; Ma, X.; Lan, Z.; Xu, W.; Wen, R. Analysis of Condensation Heat Transfer Enhancement with Dropwise-Filmwise Hybrid Surface: Droplet Sizes Effect. *Int. J. Heat Mass Transf.* **2014**, *77*, 785–794. https://doi.org/10.1016/j.ijheatmasstransfer.2014.05.052.

(64) Peng, B.; Ma, X.; Lan, Z.; Xu, W.; Wen, R. Experimental Investigation on Steam Condensation Heat Transfer Enhancement with Vertically Patterned Hydrophobic-Hydrophilic Hybrid Surfaces. *Int. J. Heat Mass Transf.* **2015**, *83*, 27–38.

https://doi.org/10.1016/j.ijheatmasstransfer.2014.11.069.

(65) Alwazzan, M.; Egab, K.; Peng, B.; Khan, J.; Li, C. Condensation on Hybrid-Patterned Copper Tubes (I): Characterization of Condensation Heat Transfer. *Int. J. Heat Mass Transf.* **2017**, *112*, 991–1004. https://doi.org/10.1016/j.ijheatmasstransfer.2017.05.039.

(66) Alwazzan, M.; Egab, K.; Peng, B.; Khan, J.; li, C. Condensation on Hybrid-Patterned Copper Tubes (II): Visualization Study of Droplet Dynamics. *Int. J. Heat Mass Transf.* **2017**, *112*, 950–958. https://doi.org/10.1016/j.ijheatmasstransfer.2017.05.040.

(67) Oestreich, J. L.; van der Geld, C. W. M.; Oliveira, J. L. G.; da Silva, A. K. Experimental Condensation Study of Vertical Superhydrophobic Surfaces Assisted by Hydrophilic Constructal-like Patterns. *Int. J. Therm. Sci.* **2019**, *135* (December 2017), 319–330. https://doi.org/10.1016/j.ijthermalsci.2018.09.024.

(68) Hou, Y.; Yu, M.; Chen, X.; Wang, Z.; Yao, S. Recurrent Filmwise and Dropwise Condensation on a Beetle Mimetic Surface. *ACS Nano* **2015**, *9* (1), 71–81. https://doi.org/10.1021/nn505716b.

(69) Ölçeroᵭlu, E.; McCarthy, M. Self-Organization of Microscale Condensate for Delayed Flooding of Nanostructured Superhydrophobic Surfaces. *ACS Appl. Mater. Interfaces* **2016**, *8* (8), 5729–5736. https://doi.org/10.1021/acsami.6b00852.

(70) Shang, Y.; Hou, Y.; Yu, M.; Yao, S. Modeling and Optimization of Condensation Heat Transfer at Biphilic Interface. *Int. J. Heat Mass Transf.* **2018**, *122*, 117–127. https://doi.org/10.1016/j.ijheatmasstransfer.2018.01.108.

(71) Xing, D.; Wang, R.; Wu, F.; Gao, X. Confined Growth and Controlled Coalescence/Self-Removal of Condensate Microdrops on a Spatially Heterogeneously Patterned Superhydrophilic-Superhydrophobic Surface. *ACS Appl. Mater. Interfaces* **2020**, *12* (26), 29946–29952. https://doi.org/10.1021/acsami.0c04922.

(72) Betz, A. R.; Xu, J.; Qiu, H.; Attinger, D. Do Surfaces with Mixed Hydrophilic and Hydrophobic Areas Enhance Pool Boiling? *Appl. Phys. Lett.* **2010**, *97* (14), 1–4. https://doi.org/10.1063/1.3485057.

(73) Motezakker, A. R.; Sadaghiani, A. K.; Çelik, S.; Larsen, T.; Villanueva, L. G.; Koşar, A. Optimum Ratio of Hydrophobic to Hydrophilic Areas of Biphilic Surfaces in Thermal Fluid Systems Involving Boiling. *Int. J. Heat Mass Transf.* **2019**, *135*, 164–174. https://doi.org/10.1016/j.ijheatmasstransfer.2019.01.139.

(74)   Van Dyke, A. S.; Collard, D.; Derby, M. M.; Betz, A. R. Droplet Coalescence and Freezing on Hydrophilic, Hydrophobic, and Biphilic Surfaces. *Appl. Phys. Lett.* **2015**, *107* (14), 141602. https://doi.org/10.1063/1.4932050.

(75)   Gao, S.; Liu, W.; Liu, Z. Tuning Nanostructured Surfaces with Hybrid Wettability Areas to Enhance Condensation. *Nanoscale* **2019**, *11* (2), 459–466. https://doi.org/10.1039/c8nr05772a.

(76)   Torresin, D.; Tiwari, M. K.; Col, D. Del; Poulikakos, D. Flow Condensation on Copper-Based Nanotextured Superhydrophobic Surfaces. *Langmuir* **2013**, *29* (2), 840–848.

(77)   Kim, S. M.; Mudawar, I. Flow Condensation in Parallel Micro-Channels - Part 2: Heat Transfer Results and Correlation Technique. *Int. J. Heat Mass Transf.* **2012**, *55* (4), 984–994. https://doi.org/10.1016/j.ijheatmasstransfer.2011.10.012.

(78)   Kim, S. M.; Kim, J.; Mudawar, I. Flow Condensation in Parallel Micro-Channels - Part 1: Experimental Results and Assessment of Pressure Drop Correlations. *Int. J. Heat Mass Transf.* **2012**, *55* (4), 971–983. https://doi.org/10.1016/j.ijheatmasstransfer.2011.10.013.

(79)   O'Neill, L. E.; Balasubramaniam, R.; Nahra, H. K.; Hasan, M. M.; Mudawar, I. Flow Condensation Heat Transfer in a Smooth Tube at Different Orientations: Experimental Results and Predictive Models. *Int. J. Heat Mass Transf.* **2019**, *140*, 533–563. https://doi.org/10.1016/j.ijheatmasstransfer.2019.05.103.

(80)   O'Neill, L. E.; Mudawar, I.; Hasan, M. M.; Nahra, H. K.; Balasubramaniam, R.; Mackey, J. R. Flow Condensation Pressure Oscillations at Different Orientations. *Int. J. Heat Mass Transf.* **2018**, *127*, 784–809. https://doi.org/10.1016/j.ijheatmasstransfer.2018.07.072.

(81)   Coleman, H. W.; Steele, W. G. *Experimentation, Validation, and Uncertainty Analysis for Engineers: Fourth Edition*; 2018. https://doi.org/10.1002/9781119417989.

(82)   Chen, X.; Kong, L.; Dong, D.; Yang, G.; Yu, L.; Chen, J.; Zhang, P. Synthesis and Characterization of Superhydrophobic Functionalized Cu(OH) 2 Nanotube Arrays on Copper Foil. *Appl. Surf. Sci.* **2009**, *255* (7), 4015–4019. https://doi.org/10.1016/j.apsusc.2008.10.104.

(83)   Kim, S.; Mudawar, I. Universal Approach to Predicting Heat Transfer Coefficient for Condensing Mini / Micro-Channel Flow. *Int. J. Heat Mass Transf.* **2013**, *56* (1–2), 238–250. https://doi.org/10.1016/j.ijheatmasstransfer.2012.09.032.

(84)   Lockhart;, R. W. M. R. C. Proposed Correlation of Data for Isothermal Two-Phase, Two-

Component Flow in Pipes. *Chem. Eng. Prog.* **1949**, *45* (1).

(85) Soliman, H. M. On the Annular-to-wavy Flow Pattern Transition during Condensation inside Horizontal Tubes. *Can. J. Chem. Eng.* **1982**. https://doi.org/10.1002/cjce.5450600405.

(86) Kim, S.; Mudawar, I. Universal Approach to Predicting Two-Phase Frictional Pressure Drop for Adiabatic and Condensing Mini / Micro-Channel Flows. *Int. J. Heat Mass Transf.* **2012**, *55* (11–12), 3246–3261. https://doi.org/10.1016/j.ijheatmasstransfer.2012.02.047.

(87) Thomas Young, B.; For Sec, M. D. III. An Essay on the Cohesion of Fluids. *Philos. Trans. R. Soc. London* **1805**, *95*, 65–87. https://doi.org/10.1098/rstl.1805.0005.

(88) Wenzel, R. N. Resistance of Solid Surfaces to Wetting by Water. *Ind. Eng. Chem.* **1936**, *28* (8), 988–994. https://doi.org/10.1021/ie50320a024.

(89) Cassie, B. D. Wettability of Porous Surfaces. **1944**, No. 5, 546–551.

(90) Lafuma, A.; Quéré, D. Superhydrophobic States. *Nat. Mater.* **2003**, *2* (7), 457–460. https://doi.org/10.1038/nmat924.

(91) Miljkovic, N.; Wang, E. N. Condensation Heat Transfer on Superhydrophobic Surfaces. *MRS Bull.* **2013**, *38* (5), 397–406. https://doi.org/10.1557/mrs.2013.103.

(92) Volmer, M.; Weber, A. Keimbildung in Übersättigten Gebilden. *Zeitschrift für Phys. Chemie* **2017**, *119U* (1), 277–301. https://doi.org/10.1515/zpch-1926-11927.

(93) Milne, A. J. B.; Amirfazli, A. Drop Shedding by Shear Flow for Hydrophilic to Superhydrophobic Surfaces. *Langmuir* **2009**, *25* (24), 14155–14164. https://doi.org/10.1021/la901737y.

(94) Antonini, C.; Carmona, F. J.; Pierce, E.; Marengo, M.; Amirfazli, A. General Methodology for Evaluating the Adhesion Force of Drops and Bubbles on Solid Surfaces. *Langmuir* **2009**, *25* (11), 6143–6154. https://doi.org/10.1021/la804099z.

(95) Mohammadpour Chehrghani, M.; Abbasiasl, T.; Sadaghiani, A. K.; Koşar, A. Copper-Based Superhydrophobic Nanostructures for Heat Transfer in Flow Condensation. *ACS Appl. Nano Mater.* **2021**, *2021*, 1719–1732. https://doi.org/10.1021/acsanm.0c03181.

(96) Ghosh, A.; Beaini, S.; Zhang, B. J.; Ganguly, R.; Megaridis, C. M. Enhancing Dropwise Condensation through Bioinspired Wettability Patterning. *Langmuir* **2014**, *30* (43), 13103–13115. https://doi.org/10.1021/la5028866.

(97) Mahapatra, P. S.; Ghosh, A.; Ganguly, R.; Megaridis, C. M. Key Design and Operating

Parameters for Enhancing Dropwise Condensation through Wettability Patterning. *Int. J. Heat Mass Transf.* **2016**, *92*, 877–883. https://doi.org/10.1016/j.ijheatmasstransfer.2015.08.106.

(98) Egab, K.; Alwazzan, M.; Peng, B.; Oudah, S. K.; Guo, Z.; Dai, X.; Khan, J.; Li, C. Enhancing Filmwise and Dropwise Condensation Using a Hybrid Wettability Contrast Mechanism: Circular Patterns. *Int. J. Heat Mass Transf.* **2020**, *154*, 119640. https://doi.org/10.1016/j.ijheatmasstransfer.2020.119640.